

Rydberg Atoms in a Ladder Geometry: Quench Dynamics and Floquet Engineering

Mainak Pal^{1,*} and Tista Banerjee^{1,†}

¹*School of Physical Sciences, Indian Association for the Cultivation of Science, Kolkata 700032, India*

In recent days, Rydberg atom quantum simulator platforms have emerged as novel quantum simulators for physical systems ranging from condensed matter to particle physics. On a fundamental level, these platforms allow for a direct test of our understanding of the emergence of quantum statistical mechanics starting from the laws of quantum dynamics. In this paper, we investigate the fate of quantum dynamics in a model of Rydberg atoms arranged in a square ladder geometry, with a Rabi frequency 2Ω and a detuning profile which is staggered along the longer direction with amplitude Δ . As the staggering strength Δ is tuned from $\Delta/\Omega = 0 \rightarrow \infty$, the model exhibits a wide class of dynamical phenomena, ranging from (i) quantum many-body scars (QMBS) ($\Delta/\Omega \sim 0, 1$), (ii) integrability induced slow dynamics and approximate Krylov fractures ($\Delta/\Omega \gg 1$). Additionally, by leveraging the underlying chiral nature of the spectrum of this model Hamiltonian, it is possible to design Floquet protocols leading to dynamical signatures reminiscent of discrete time-crystalline order and exact Floquet flat bands. Finally, we study the robustness of these dynamical features against imperfections in the implementation of the Floquet protocols, long-range van der Waals interactions and inevitable influences from the environment in the form of pure dephasing and the finite lifetime of the Rydberg excited state.

I. INTRODUCTION

Over the past decade, Rydberg atom quantum simulators [1–7] have become a versatile testbed to study fundamental aspects of quantum matter. On one hand, it can sharpen our understanding of strongly interacting quantum matter ranging from quantum many-body systems [8] to lattice gauge theories [9] via the inspection of quantum phase transition [2, 4, 7], different topological phases [10], the stability of quantum matter [11] and effects of different decoherence mechanisms [1] inevitable in such experimental platforms. On the other hand, due to advancement of technologies in controlled state preparation [12, 13], it can also be helpful in demonstrating the equilibration processes of an out-of-equilibrium initial state in such synthetic quantum platform and generation of new quantum phases of matter away from equilibrium [2, 7].

In this paper our focus will be to understand the nature of the out-of-equilibrium properties of such many-body quantum systems. In generic isolated interacting many-body quantum systems, where the total energy is the only conserved quantity, it is expected that any out-of-equilibrium initial state relaxes quickly to a late-time thermal equilibrium which is entirely controlled by the initial energy density of the state with respect to the underlying Hamiltonian [14]. This kind of thermal equilibrium achieved via a completely unitary quantum evolution, can be understood within the paradigm of the eigenstate thermalization hypothesis (ETH) [14–17]. However, it was shown in [2] that under certain circumstances, even simple initial states evolving

via a generic Hamiltonian, may fail to thermalize in the above sense: certain initial states (for e.g., charge density wave states of various periods) undergo persistent oscillations, evading thermalization within the time scales up to which coherent unitary evolution could be maintained. Consequently, these many-body oscillations were attributed to the presence of quantum many-body scars (QMBS) [18, 19] — these are eigenstates of the Hamiltonian which have a considerable overlap with these initial states and they are almost equidistant in energy, giving rise to an almost single frequency oscillation. The phenomena of appearance of quantum many-body scars in the Rydberg atom quantum simulator platform in the so called Rydberg blockade regime [20] (i.e., no two neighboring atoms can be simultaneously in the Rydberg excited state due to high energy penalty) can be most easily understood within the realm of the paradigmatic PXP model [18, 19]. Furthermore, it was shown in [21] that by leveraging an underlying chirality operator, which manifests itself as a many-body π -pulse, one can design Floquet protocols which leads to the realization of a period-two discrete time crystalline order, stabilized by the presence of QMBS. It is worth emphasizing here, that the presence of this chirality operator which anticommutes with the Hamiltonian but commutes with the spatial reflection symmetry operators associated with the Hamiltonian, imply the existence of an exponentially large number of exact zero modes which are protected by an index theorem [22].

The Rydberg atom platforms offer a remarkable degree of tunability in the arrangement of the atoms and external LASER induced light-matter interactions [6]. Owing to this tunability, it becomes relevant and also interesting to ask how do the above features such as the presence of quantum many-body scars and sub-harmonic response manifest themselves when the atoms are placed in a more sophisticated arrangement. To explore this,

* intdydx@gmail.com

† banerjeemou09@gmail.com

we focus on an arrangement of the Rydberg atoms on a 2-leg square ladder geometry (see Fig. 1), which aims to understand the properties of two closely spaced Rydberg chains, with mutual separation smaller than the radius of the Rydberg blockading. It is well known, that a PXP model on any bipartite lattice with zero detuning, preserves the structure of the chirality operator [21], which means that in the 2-leg square ladder geometry we also have this chirality operator, hence the spectral reflection symmetry and the exponentially large number of exact zero modes follow immediately. Furthermore, in experiments it is also possible to implement site-dependent detuning profiles [2, 4, 23], however, in this case it is no longer guaranteed that the above features such as the existence of a chirality operator and exponentially large number of exact zero modes, will be preserved under an arbitrary detuning profile. In this regard [24] have been able to identify a simple staggered detuning profile (see Fig. 1) which preserves these desirable features and leads to the presence of quantum many-body scars which are qualitatively different in nature compared to that of the paradigmatic PXP chain.

In this paper, we analyzed the dynamical features in a model of Rydberg atoms arranged in a square ladder geometry with a detuning profile which is staggered along the longer direction. The ground-state and the Rydberg excited state is off-resonantly coupled via lasers with Rabi frequency 2Ω . We find that tuning the strength of such staggered detuning (denoted as Δ) results in a broad range of dynamical phenomena. As pointed out in [24] this model hosts quantum many-body scars (QMBS) ($\Delta/\Omega \sim 0,1$) while the qualitative nature of these scars at $\Delta = 1$ are very different from those at $\Delta = 0$. This model also features slow dynamics and approximate Krylov fractures induced by approximate emergent integrability arising for $\Delta/\Omega \geq 2.5$ which is a consequence of the low-energy effective Hamiltonian up to second-order being exactly integrable and higher order non-integrable contributing very weakly in this parameter regime and the particular form of the second-order effective Hamiltonian allows us to explicitly write down an extensive number of emergent conserved charges.

Apart from such a rich structure in the quench dynamics in this system, by leveraging the underlying chiral nature of the spectrum of the Hamiltonian, we have been able to design Floquet protocols leading to dynamical signatures reminiscent of discrete-time-crystalline order and exact Floquet flat bands. We have also studied the robustness of these different class of dynamical phenomena against the possible imperfections in the implementation of the Floquet protocols. Finally, we take into account how the presence of long-range van der Waals repulsive interactions (which are present in the actual experimental set up) influences the existence of quantum many-body scars by inspecting the validity of assuming such a non-perturbative generalization of the paradigmatic PXP model in a square-ladder geometry

to be the low-energy effective description of the full long-range interacting system. We have also discussed the influence of environmental loss channels on the emergent conservation laws and quantum many-body scars by considering a finite lifetime for the Rydberg excited states and the loss of phase-coherence (pure-dephasing). Though for we mostly focus on results obtained for atoms arranged in a square-ladder geometry with staggered detuning in the longer direction, these results can be easily generalizable for multiple-leg ladder and 2D square geometry with staggered detuning along the horizontal direction. These generalizations have been discussed briefly in the appendices (see Appendix-D for discussion on 3-leg ladders and Appendix-E3 for discussion on two dimensional square lattice).

The rest of this paper is organized as follows: in Sec. II we present the details of the system we study, focusing on introducing the Rydberg ladder model Hamiltonian $\hat{\mathcal{H}}$, and the associated chirality operators $\hat{C}_{1,2}$. In Sec. III we briefly recapitulate the existing results (Sec. III A) associated with the system under consideration (for a detailed discussion see [24]). Next, we focus on the emergent integrability induced slow dynamics (Sec. III B) in the regime of large staggered detuning with a special emphasis on the appearance of extensive number of emergent conservation laws and their imprints on the short-range spectral correlations. The existence of approximately conserved operators in addition to the exactly conserved total energy, imply that starting from any simple initial state the system should relax to a generalized Gibbs ensemble for intermediate times, and ultimately relax to the Gibbs ensemble only after a sufficient amount of time which is set by the strength of the higher-order integrability breaking terms. We have shown that starting from a one Rydberg excitation state, the system relaxes rapidly to a generalized Gibbs ensemble (defined by initial values of the exact and approximate conserved charges) and does not show any deviation from this ensemble till the time scales probed via numerical simulations. Next, in Sec. IV, we discuss the existence and stability of exact revivals from any initial state by designing two different classes of Floquet protocols realized by leveraging the chirality operators associated with the model under consideration. Our results show that the evolution using one of the Floquet protocols (Sec. IV A) leads to a state-dependent subharmonic response i.e., the time-period of the subharmonic response depends on the periodicity of the initial state with respect to the associated lattice-translation operators. We also present results considering another class of Floquet protocol (Sec. IV B) that gives rise to exact revivals under the action of every one-cycle of the Floquet unitary, starting from any initial state in the presence of non-zero staggered detuning. Lastly, in Sec. V we analyze the stability of QMBS (Sec. V A) and emergent conservation laws (Sec. V B) in the presence of spontaneous emission from the Rydberg excited state and pure-dephasing by considering the

Lindblad (or, Gorini–Kossakowski–Sudarshan–Lindblad) master equation as an equation of motion mimicking such effects. Our results indicate that although the persistent oscillations in the fidelity dynamics starting from the Néel state are unstable against both decoherence mechanisms considered, the Lindblad evolution describing the spontaneous emission, starting from all the atoms in the Rydberg ground-state (Rydberg vacuum state) shows persistent oscillations where the amplitude and frequency of such oscillation closely follows the dynamics generated by the unitary evolution to a short time scale. On the other hand, the emergent conservation laws starting from generic initial states are more stable against dephasing and persist for longer time durations.

II. MODEL

In this paper, we focus on the nature of out-of-equilibrium quantum dynamics in the model governed by the Hamiltonian (1). This model is a non-perturbative generalization of the paradigmatic PXP chain [18, 19, 25], to the case of a 2-leg square ladder geometry with a site-dependent detuning which is staggered along the longer direction.

$$\hat{H} = \Omega \sum_{j=1}^L \sum_{a=1}^2 \hat{P}_{j-1,a}^\downarrow \hat{P}_{j+1,a}^\downarrow \hat{P}_{j,a}^\downarrow \hat{\sigma}_{j,a}^x - \Delta \sum_{j=1}^L \sum_{a=1}^2 (-1)^j \hat{\sigma}_{j,a}^z \quad (1)$$

Here $\hat{\sigma}_{j,a}^\alpha$ are spin- $\frac{1}{2}$ operators at site (j,a) , with $j = 1, 2, \dots, L$, $a = 1, 2$ and $\alpha = x, y, z$. The operators $\hat{P}_{j,a}^\downarrow = (1 - \hat{\sigma}_{j,a}^z)/2$ are local projection operators onto the spin-down state ($|\downarrow\rangle_{j,a}$) or the Rydberg ground-state ($|\circ\rangle_{j,a}$) at site (j,a) . For brevity, we use the notation $\hat{\hat{\sigma}}_{j,a}^\alpha = \hat{P}_{j-1,a}^\downarrow \hat{P}_{j+1,a}^\downarrow \hat{P}_{j,a}^\downarrow \hat{\sigma}_{j,a}^\alpha$ and for later convenience, we also denote the diagonal and off-diagonal parts of the Hamiltonian (in the computational basis) as $\hat{H}_z = -\Delta \sum_{j=1}^L \sum_{a=1}^2 (-1)^j \hat{\sigma}_{j,a}^z$ and $\hat{H}_x = \Omega \sum_{j=1}^L \sum_{a=1}^2 \hat{\hat{\sigma}}_{j,a}^x$ so that $\hat{H} = \hat{H}_x + \hat{H}_z$. In the language of Rydberg atom quantum simulator platforms [2, 4, 23], the Rabi frequency is 2Ω and the detuning on the site (j,a) is $(-1)^j \Delta$. For this entire paper, we fix $\Omega = 1$, and vary Δ to access different dynamical regimes of the model.

The generalization of the PXP chain ($\hat{H}_{\text{PXP}} = -\Omega \sum_{j=1}^L \hat{\sigma}_j^x$) to the model (1) preserves some important features found in the PXP chain such as (i) reflection symmetry of the spectrum of the Hamiltonian and (ii) exponentially large number of zero modes protected by an index theorem. Both of these properties can be understood by considering the (chirality) operators $\hat{C}_{1,2}$ which anti-commute with the Hamiltonian.

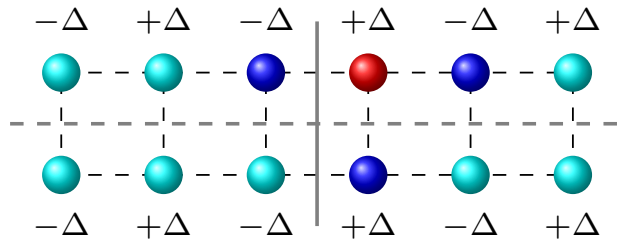


FIG. 1. A schematic representation of the 2-leg Rydberg (square) ladder setup with $N = 2L = 12$ atoms and a staggered detuning profile ($\Delta_{j,a} = (-1)^j \Delta$). The solid and dashed gray lines shows various cuts and spatial reflection symmetry axes for future convenience. The kinetic constraint i.e., the strong Rydberg blocked regime is illustrated as follows: if one atom is in the $|\bullet\rangle \equiv |\uparrow\rangle$ state (Rydberg excited state, denoted by the red sphere), then all its neighboring atoms must be in the $|\circ\rangle \equiv |\downarrow\rangle$ state (denoted by blue spheres) and cannot be flipped to the $|\bullet\rangle$ state under the action of the Hamiltonian (1).

$$\hat{C}_1 = \hat{T}_x \hat{C} \quad (2)$$

$$\hat{C}_2 = \hat{T}_x \hat{T}_y \hat{C} \quad (3)$$

$$\{\hat{C}_{1,2}, \hat{H}\} = 0 \quad (4)$$

$$\hat{C} = \prod_{j=1}^L \prod_{a=1}^2 \hat{\sigma}_{j,a}^z \quad (5)$$

Here $\hat{T}_{x,y}$ denote the lattice-translation operators by one unit along the longer and the shorter directions respectively. Eq. (4) implies that if $|E\rangle$ is an eigenstate of the Hamiltonian (1) with eigenvalue E , then $\hat{C}_{1,2} |E\rangle$ is also an eigenstate of (1) with eigenvalue $-E$. For this reason we shall refer to $\hat{C}_{1,2}$ as chirality operators. Moreover, as the Hamiltonian \hat{H} and the chirality operators $\hat{C}_{1,2}$ both commute with the spatial reflection operation about the vertical cut (solid gray line in Fig. 1), it follows from [22] that the Hamiltonian (1) has exponentially large number (in system size N) of exact mid-spectrum zero modes which are protected by an index theorem, for any value of Δ .

Since the model (1) shares a number of key features with the paradigmatic PXP chain, it interesting to ask whether the non-equilibrium dynamics of (1) shows any anomalous behavior similar to the quantum many-body scars [2, 18, 19] or discrete time crystalline order observed in the periodically kicked PXP chain [21]. A part of this question was answered in [24], where the quantum many-body scarring phenomenology of this model was studied for $\Delta/\Omega \in [0, 1]$. Our goal in this paper is to present evidence of further anomalous dynamical behavior both in the quench dynamics for a range of parameters, and to engineer Floquet protocols leading to dynamical signatures reminiscent of discrete

number of conservation laws: $\hat{Z}_\pi = \sum_{j,a} (-1)^j \hat{\sigma}_{j,a}^z$ and $\hat{Q}_j = \hat{\sigma}_{j,1}^z \hat{\sigma}_{j,2}^z$, $\forall j = 1, 2, \dots, L$. The presence of these additional conservation laws can be understood by considering the action of $\hat{\mathcal{H}}_{\text{eff}}^{(2)}$ on the Fock states: the terms in the second summation of Eq. (6) essentially perform “blockaded spin-flips” i.e. $|\dots \overset{\circ}{\sigma}_{j-1}^{\circ j-1} \overset{\bullet}{\sigma}_{j-1}^{\circ j+1} \dots\rangle \leftrightarrow |\dots \overset{\circ}{\sigma}_{j-1}^{\circ j-1} \overset{\bullet}{\sigma}_{j-1}^{\circ j+1} \dots\rangle$ where the “blockade” is due to the $\hat{\mathcal{P}}^\downarrow$ projectors at sites $j \pm 1$ on both legs of the ladder. This leads to the realization of an effective two-level oscillation of a Rydberg excitation between the two legs of the j^{th} rung, provided that this rung is “blockaded” appropriately by $|\circ\rangle$ states

$$\hat{\mathcal{H}}_{\text{eff}}^{(2)} = -\frac{\Omega^2}{2\Delta} \sum_{j=1}^L \sum_{a=1}^2 (-1)^j \hat{\sigma}_{j,a}^z - \frac{\Omega^2}{4\Delta} \sum_{j=1}^L \sum_{a=1}^2 (-1)^j \hat{\mathcal{P}}_{j-1,a}^\downarrow \hat{\mathcal{P}}_{j-1,\bar{a}}^\downarrow \hat{\mathcal{P}}_{j+1,a}^\downarrow \hat{\mathcal{P}}_{j+1,\bar{a}}^\downarrow \hat{\mathcal{P}}_{j,a}^\downarrow \left(\hat{\sigma}_{j,a}^x \hat{\sigma}_{j,\bar{a}}^x + \hat{\sigma}_{j,a}^y \hat{\sigma}_{j,\bar{a}}^y \right) \quad (6)$$

We find that the third-order effective Hamiltonian vanishes exactly and the next non-trivial contribution comes from the fourth-order of the perturbation theory and is non-integrable. However, the strength of this integrability breaking term is $\sim \Omega^3/\Delta^4$ and contributes very weakly for the parameter range $\Delta/\Omega \geq 2$.

The fact that the second-order perturbative Hamiltonian $\hat{\mathcal{H}}_{\text{eff}}^{[2]}$ remains exactly integrable, has certain consequences in the short range spectral correlations of the system as well as on the relaxation dynamics from certain non-equilibrium initial states. As a measure of short-range spectral correlations we have used the distribution of the ratio (r_n) of consecutive level spacings (s_n), defined as $r_n = \min(s_n, s_{n-1})/\max(s_n, s_{n-1})$ where $s_n = E_{n+1} - E_n$ denotes the gap between n -th and $(n+1)^{\text{th}}$ energy level [27]. At values of $\Delta \sim 2\Omega$, due to the strength of the integrability breaking term being weak, the consecutive level-spacing-ratio distribution ($P(r)$) resembles a Poissonian nature (see Fig. 4 top right panel). For $\Delta \sim \Omega$ (see Fig. 4 top left panel), $P(r)$ exhibits level repulsion which is a consequence of the fact that the fourth-order integrability breaking terms are not weak and the effective Hamiltonian now becomes non-integrable at this coupling. As Fig. 3 (right panel) demonstrates, the full spectrum of $\hat{\mathcal{H}}_{\text{eff}}^{[2]}$ and that of the full Hamiltonian $\hat{\mathcal{H}}$ (both obtained via numerical exact diagonalization), agree very well for $\Delta \sim 3\Omega$, whereas for $\Delta \sim \Omega$ (Fig. 3 (left panel)) one needs to consider higher order processes (such as $\hat{\mathcal{H}}_{\text{eff}}^{[4]}$, obtained via numerical perturbative SW rotation [28]) to capture the spectral features of the full Hamiltonian $\hat{\mathcal{H}}$.

The *emergent integrability* is not related to any lattice symmetries of the Hamiltonian (1). This can be verified from the spectral analysis of the many-body energy levels of a modified Hamiltonian (see Eq. (7)) having weak onsite disorder on top of the perfectly staggered detuning

at surrounding sites. There are few simple consequence of this blockaded spin-flipping process, namely (i) Fock states such as the Néel state and the Rydberg vacuum state remain completely frozen and (ii) the expectation value of the operators $\hat{Q}_j = \hat{\sigma}_{j,1}^z \hat{\sigma}_{j,2}^z$ $\forall j = 1, 2, \dots, L$ remain conserved under the action of the second-order effective Hamiltonian. All eigenstates of $\hat{\mathcal{H}}_{\text{eff}}^{(2)}$ can be labeled by the quantum numbers corresponding to these conserved quantities, and a recipe of such an enumeration procedure is given in Appendix-C1.

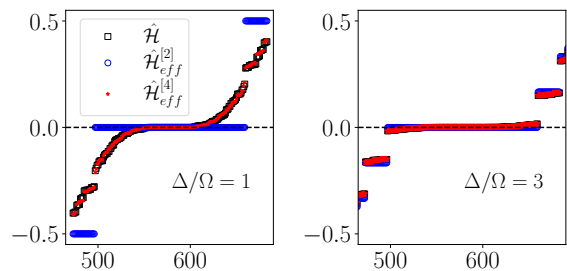


FIG. 3. Comparison of the spectrum of $\hat{\mathcal{H}}$ (black squares), $\hat{\mathcal{H}}_{\text{eff}}^{[2]}$ (blue circles) and $\hat{\mathcal{H}}_{\text{eff}}^{[4]}$ (red stars) [28] for $\Delta/\Omega = 1$ (left panel) and $\Delta = 3\Omega$ (right panel) with $N = 16$ atoms (only the middle part of the spectrum is shown). This illustrates the fact that $\hat{\mathcal{H}}_{\text{eff}}^{[2]}$ can explain the lack of level repulsion for $\Delta \sim 3\Omega$, while for understanding the level repulsion nature of the exact spectrum at $\Delta \sim \Omega$, higher order processes (i.e. consideration of $\hat{\mathcal{H}}_{\text{eff}}^{[4]}$) become important (see text for details).

profile.

$$\hat{\mathcal{H}}_{\text{dis}} = \sum_{j=1}^L \sum_{a=1}^2 \Omega \hat{\sigma}_{j,a}^x - \sum_{j=1}^L \sum_{a=1}^2 (-1)^j (\Delta + \eta \mathcal{R}_j) \hat{\sigma}_{j,a}^z \quad (7)$$

Here, $\mathcal{R}_j, \forall j = 1, 2, \dots, L$ are uniformly distributed random numbers between 0 and 1 and η is the strength of the disorder. Such a disordered Hamiltonian (7) does not possess any lattice symmetries, but nevertheless the disorder-averaged mean consecutive level spacing ratio $\langle r \rangle$ becomes close to $2 \ln 2 - 1 \sim 0.386$ for $\Delta/\Omega \sim 2$ or greater which indicates a Poissonian level statistics at these couplings (see Fig. 4 bottom panel). The observed Poissonian nature of the spectral statistics can be attributed to the existence of extensive number of approximate emergent conservation laws.

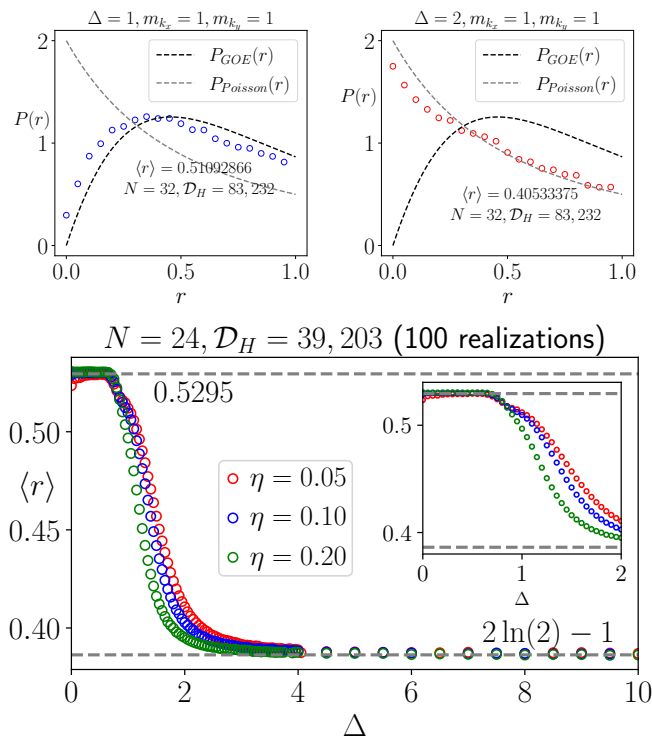


FIG. 4. Top panels: Distribution of consecutive level spacing ratio statistics ($P(r)$) for $\Delta/\Omega = 1$ (left panel) and $\Delta/\Omega = 2$ (right panel) resolving translation symmetries along longer and shorter direction of Fig. 1 with translations quantum numbers $m_{k_x} = 1$ (longer direction) and $m_{k_y} = 1$ (shorter direction). In both the figures black dashed line stands for gaussian orthogonal ensemble (GOE) statistics and gray dashed line stands for Poissonian statistics. Bottom panel: Disorder averaged mean consecutive level spacing ratio $\langle r \rangle$ as a function of staggered detuning strength Δ for $N = 24$ sites ($\mathcal{D}_H = 39, 203$) averaged over 100 realizations for each Δ, η . Three different colors indicate three different disorder strengths $\eta = 0.05$ (red circles), $\eta = 0.1$ (blue circles) and $\eta = 0.2$ (green circles). As shown, $\langle r \rangle$ changes from ~ 0.5295 (GOE) to $2 \ln(2) - 1 \approx 0.386$ (Poissonian) very rapidly in between $\Delta/\Omega = 0$ and $\Delta/\Omega = 2$. The emergent integrability is achieved for $\Delta/\Omega \sim 3$. Inset of the figure describes variation of $\langle r \rangle$ as the detuning is varied in range $0 < \Delta < 2$.

For $\Delta \sim 2\Omega$ and beyond, the strength of $\hat{\mathcal{H}}_{\text{eff}}^{[4]}$ becomes negligible and the evolution of the approximately conserved charges $\hat{Q}_j, \forall j = 1, 2, \dots, L$, under the full Hamiltonian becomes more constrained near their initial values. As a consequence, certain initial states (which can be labeled by the eigenvalues of $\{\hat{Q}_j\}$, say $\{q_j\}$), exhibit exceptionally slow dynamics, as can be seen in Fig. 5 where the instantaneous expectation values of these operators under the full Hamiltonian i.e. $\{\langle Q_j(t) \rangle\}$ remain close to their initial values for very long times. For quench dynamics from such initial states, observables should in general relax to a generalized Gibbs ensemble (GGE) when an extensive number of exact conservation laws are present. In contrast in the absence of any such exact

conservation laws, the system should eventually relax to the Gibbs ensemble (GE). The exact quantum dynamics of the model (1) illustrates that in this system, where the emergent conservation laws are approximate and not exact, the exact quantum dynamics still fails to relax to the appropriate GE and remains very well describable to extremely late times via GGE (till time scales set by the fourth order effective Hamiltonian). This is illustrated in Fig. 6, where we show the late-time relaxation of a one-body operator ($h_{j,a} \equiv \hat{\sigma}_{j,a}^z - \hat{\sigma}_{j,a}^x$) for $N = 12$ and $N = 16$ atoms at $\Delta = 0, 5\Omega$ starting from a one-particle product state i.e. $|1P\rangle = |\bullet\circ\circ\circ\circ\circ\circ\rangle$. For $\Delta \sim 0$, only the total energy i.e. $\langle \psi(t) | \hat{\mathcal{H}} | \psi(t) \rangle$ is an exactly conserved quantity, and hence, the system should relax to the corresponding Gibbs ensemble with the appropriate temperature. In contrast, for $\Delta \gg \Omega$, or in this case $\Delta = 5\Omega$, as there are an extensive number of (approximate) conservation laws, the system fails to relax to the Gibbs ensemble for long times. Instead, the system relaxes to a GGE defined by the Lagrange multipliers corresponding to all the conserved charges (exact or approximate). These Lagrange multipliers are determined by requiring that the initial values of all the conserved charges be equal to the expectation value of the operators with respect to the GGE (see Appendix C)

In Fig. 7 we show the variation with Δ/Ω of the infinite-time average and the Gibbs ensemble ETH values of the quasi-conserved charges. We consider the following states: $|\text{vac}\rangle \equiv |\circ\circ\circ\circ\circ\circ\rangle$ (blue open circles), $|\mathbb{Z}_2\rangle \equiv |\bullet\circ\circ\circ\circ\bullet\rangle$ (magenta open circles), $|4P\rangle \equiv |\bullet\circ\circ\circ\bullet\circ\circ\rangle$ (green open circles), $|2P\rangle \equiv |\circ\circ\bullet\circ\circ\circ\rangle$ (orange open circles), $|\mathbb{Z}_4\rangle \equiv |\bullet\circ\circ\circ\bullet\circ\circ\rangle$ (brown open circles) in the main panel and in the inset $|\mathbb{Z}_4^{(1)}\rangle \equiv |\circ\bullet\circ\circ\bullet\circ\circ\rangle$ (red open circles). For all states in the main panel, the energy expectation value is zero, which combined with the fact that the spectrum of (1) has a reflection symmetry at any $\Delta \neq 0$, implies that all of these states should relax to the infinite temperature ($\beta = 0$) Gibbs ensemble if they achieve a thermal equilibrium. The ETH value of the quasi-conserved charges (dashed gray line) for $\beta = 0$ is very close to zero ($= 1/\mathcal{D}_H$, \mathcal{D}_H being the Hilbert space dimension). For the state $|\mathbb{Z}_4^{(1)}\rangle$ the energy expectation value is not zero ($\langle \mathbb{Z}_4^{(1)} | \hat{\mathcal{H}} | \mathbb{Z}_4^{(1)} \rangle = -L\delta$) and hence, $\beta \neq 0$. This in turn implies that the ETH value of the quasi-conserved charges corresponding to this state depend on the value of Δ/Ω shown as black dashed line, while the infinite-time average values are given as open red circles. This figure illustrates the fact that for certain initial states with zero energy density, corresponding to the infinite temperature Gibbs ensemble, the infinite-time average value drifts from the ETH value as Δ/Ω is increased from $\Delta = 0$ signaling a form of ETH violation. For other states the ETH and the infinite-time average value coincide, implying that these states do not violate ETH.

Moreover, some special initial states, growth of the

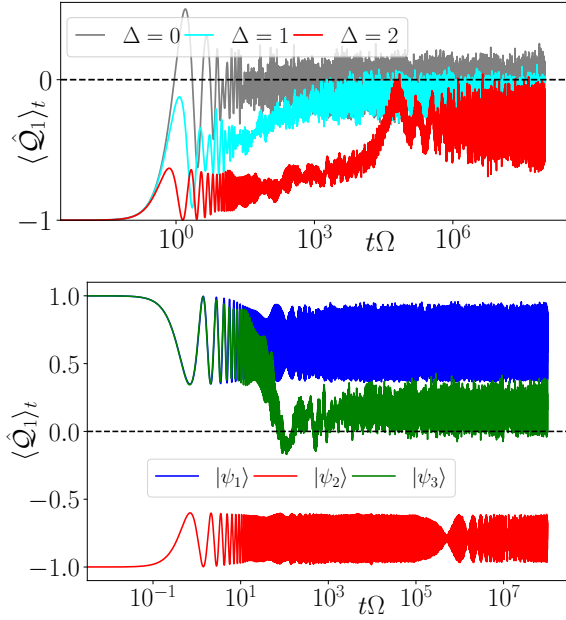


FIG. 5. Top panel: Illustration of slow evolution of one of the approximate emergent conserved charges ($\langle \hat{Q}_1 \rangle = \langle \hat{\sigma}_{1,1}^z \hat{\sigma}_{1,2}^z \rangle$) as a function of time ($t\Omega$) under the full Hamiltonian (1) at various values of Δ starting from the initial state $|\bullet\circ\circ\circ\circ\circ\circ\rangle$ for $N = 16$ atoms. Different colors indicate different values of Δ : gray solid line ($\Delta = 0$), cyan solid line ($\Delta = 1\Omega$) and red solid line ($\Delta = 2\Omega$) respectively. Bottom panel: Illustration of slow dynamics from other initial states at $\Delta = 2\Omega$. Three initial states are $|\psi_1\rangle \equiv |\mathbb{Z}_2\rangle$ (blue solid line), $|\psi_2\rangle \equiv |\text{vac}\rangle$ (blue solid line) and $|\psi_3\rangle \equiv |\circ\circ\circ\circ\circ\circ\rangle$ (green solid line). All initial states shown in both the panels are infinite temperature states, and the ETH predicted GE value of $\hat{Q}_1 = \hat{\sigma}_{1,1}^z \hat{\sigma}_{1,2}^z$ for all of them is zero (denoted by the dashed black line). In all cases the state has been evolved via ED method.

correlations is extremely slow along the horizontal bonds. This is evident from Fig. 8 where the mutual information content (for definition see Appendix-B) of the horizontal ($\mathcal{I}_{1,2}$) and the vertical bond (\mathcal{I}_{1,L_x}) are shown as a function of time for the $|\text{IP}\rangle$ state (i.e. $|\bullet\circ\circ\circ\circ\circ\rangle$) for $\Delta = 4\Omega$ for $N = 16$ atoms. While for the horizontal bond the mutual information remains close to zero, for the vertical bond it shows large time-period oscillations. Such contrasting behaviors along the two directions can be traced back to the fact that for large enough Δ/Ω , an effective Rabi flip-flop takes place which is almost exact: $|\bullet\circ\circ\circ\circ\rangle \leftrightarrow |\circ\bullet\circ\circ\rangle$. Such slow dynamics, along with the existence of simple local quasi-conserved charges $\{g_j\}$ could in principle, be utilized to store $L/2$ “classical” bits of information on a ladder of $N = 2L$ atoms (see Appendix C).

As a consequence of these approximate conservation laws which influence the quench dynamics of the system even for $\Delta \sim 2\Omega$, the bipartite von Neumann entanglement entropy $\mathcal{S}(|E\rangle)$ (see Appendix-B) of the eigenstates $|E\rangle$ of the Hamiltonian (1), shows a broad

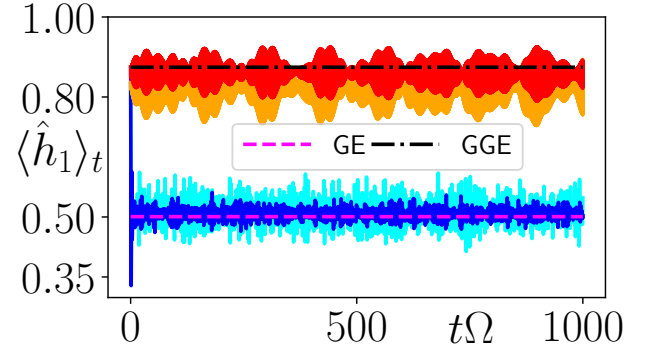


FIG. 6. Illustration of the relaxation to different ensembles for two different values of Δ/Ω and system sizes starting from the $|\text{IP}\rangle \equiv |\bullet\circ\circ\circ\circ\circ\rangle$ state. The dashed lines represent values of $\langle \hat{h}_{1,1}(t) \rangle$ (a one-body operator, see text for details) predicted from GE (magenta dashed line) and GGE (black dashed line) (see Appendix-C 3). The solid lines represent the results of the evolution under the full Hamiltonian (1) for (i) $\Delta = 0$ (blue solid line represents $N = 16$ atoms, cyan solid line represents $N = 12$ atoms) and (ii) $\Delta = 5\Omega$ (red solid line represents $N = 16$ atoms, orange solid line represents $N = 12$ atoms). In all cases the state has been evolved via ED method.

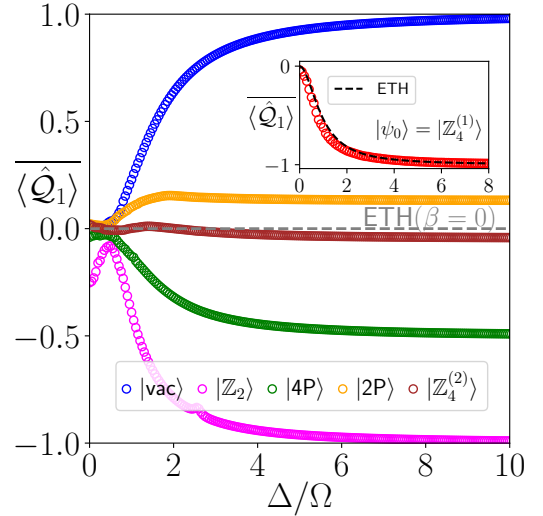


FIG. 7. In this figure we show the variation of the infinite-time average value $\langle \hat{Q}_1 \rangle$ and the corresponding Gibbs ensemble values predicted by ETH for the quasi-conserved charges with Δ/Ω starting from different initial states $|\psi_0\rangle$. For the main panel the states considered are $|\text{vac}\rangle$ (blue open circles), $|\mathbb{Z}_2\rangle$ (magenta open circles), $|\mathbb{4P}\rangle$ (green open circles), $|\mathbb{2P}\rangle$ (orange open circles), $|\mathbb{Z}_4^{(2)}\rangle$ (brown open circles) which all have zero energy. At late times, these states should relax to the $\beta = 0$ Gibbs ensemble and the ETH value for the quasi-conserved charges is zero (denoted by the dashed gray line). For the inset we consider the state $|\mathbb{Z}_4^{(1)}\rangle$ which does not have zero energy and hence the ETH values of the quasi-conserved charges depend on Δ/Ω (dashed black line). The corresponding infinite-time average values are shown in the inset (red open circles). See text for details.

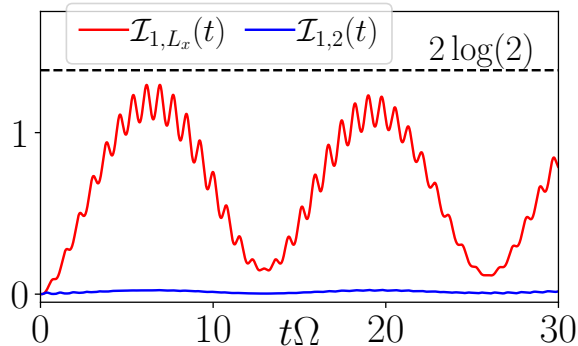


FIG. 8. Time evolution of mutual information along horizontal (blue solid line) and vertical (red solid line) nearest neighbour bonds for the $|1P\rangle$ state (i.e. $|\bullet^{\circ}\dots^{\circ}\circ\rangle$) for $\Delta = 4\Omega$ for $N = 16$ atoms. The maximum possible value attainable for the mutual information is $2\log(2)$ (denoted by the black dashed line) which is realized for ideal Rabi flip-flops $|\bullet^{\circ}\dots^{\circ}\circ\rangle \leftrightarrow |\circ^{\circ}\dots^{\circ}\bullet\rangle$ (see text for details). The state has been evolved using a discrete time-step integrator [29].

distribution across the entire range of the spectrum (see Figs. 9,10). We have checked numerically that the eigenstates close to the middle of the spectrum obey volume law, but the coefficients corresponding to these volume law scalings have a broad distribution. This can be taken as a signature of an *approximate* Krylov fracture taking place due these approximate emergent conservation laws. In Appendix-C, we have analytically constructed all eigenstates of the second-order effective Hamiltonian $\hat{\mathcal{H}}_{\text{eff}}^{[2]}$. These eigenstates have simple “Bell-pair” like states embedded in some of the rungs, while the other rungs remain completely unentangled when the entanglement entropy is measured across the vertical cut (henceforth denoted as UD cut), designated as dashed gray line in Fig. 1. Such a structure can help us in understanding, to some degree, the nature of the bi-partite von Neumann entanglement entropy of the eigenstates of the full Hamiltonian at $\Delta = 2\Omega$. We note here that this only explains the entanglement from the UD cut. The entanglement entropies across the left-right bi-partition (henceforth denoted as LR cut) are exactly zero for all the analytically constructed eigenstates (labeled by a collection of conserved charges $\{z_{\pi}, q_1, q_2, \dots, q_L\}$ of $\hat{\mathcal{H}}_{\text{eff}}^{[2]}$). However, as these eigenstates are highly degenerate, we suspect that a full numerical diagonalization scheme which is unaware of such approximate symmetries, outputs arbitrary hybridizations of these analytically constructed eigenstates, leading to a non-zero values of entanglement entropies for the eigenstates across the LR cut. The finite bandwidth of the tower of states in Figs. 9(d) and 10(d) are due to the influence of higher order processes, and can be captured quantitatively via $\hat{\mathcal{H}}_{\text{eff}}^{[4]}$ (see Fig. 3(b)). That being said, at this moment we do not have any understanding of

the eigenstates of $\hat{\mathcal{H}}_{\text{eff}}^{[4]}$ from an analytical point of view, as the construction and diagonalization of $\hat{\mathcal{H}}_{\text{eff}}^{[4]}$ were performed using numerical schemes.

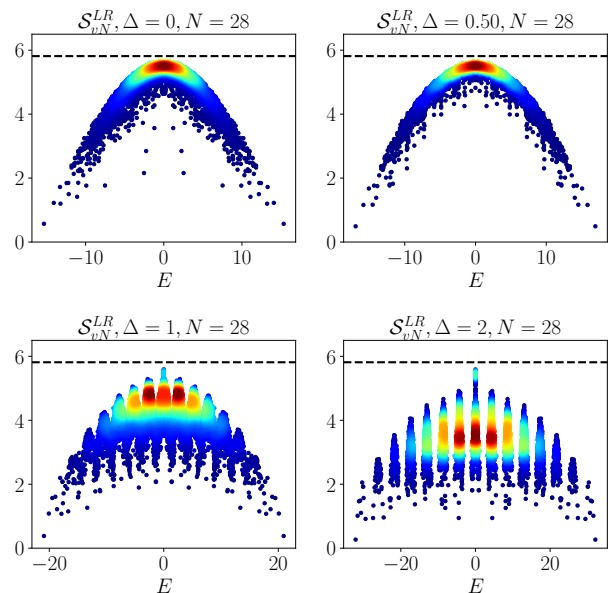


FIG. 9. Bipartite von Neumann entanglement entropy (for definition see Appendix B) of all many-body eigenstates of the Hamiltonian with respect to the LR partition at $\Delta/\Omega = 0$ (top left panel), $\Delta/\Omega = 0.5$ (top right panel), $\Delta/\Omega = 1$ (bottom left panel) and $\Delta/\Omega = 2$ (bottom right panel) respectively for $N = 28$ atoms in the $k_x = k_y = 0$ sector. The solid dashed black line denotes the Page value (i.e. the average entanglement entropy of Haar-random states) in this specific symmetry sector. The broad distribution of values of entanglement entropies for $\Delta/\Omega = 1, 2$ suggest that there is a Krylov fracture of the Hilbert space, albeit approximate.

We end this section by noting that the system governed by the Hamiltonian Eq. (1) is integrable only at $\Delta/\Omega \rightarrow \infty$. For large but finite values of Δ , starting from any initial state system in the thermodynamic limit will eventually relax to the Gibbs ensemble with the effective inverse temperature β is set by the initial energy density. To understand the onset of thermalization and the finite size effects we have studied the the behavior of adiabatic gauge potential (AGP) for different system sizes N for various values of Δ/Ω . It has been argued in earlier works [30], that the scaling behavior of the norm of the regularized AGP is an extremely sensitive indicator of quantum chaos, and can detect its onset even in circumstances where widely used alternative probes such as the mean consecutive level spacing ratio [27] fails to do so. The scaling behavior of the regularized AGP can correctly predict the onset of quantum chaos even for very modest system sizes as this directly probes features of a many-body Hamiltonian at time scales which are exponentially large in system size. In Appendix F we have considered this sensitive indicator of quantum chaos, and

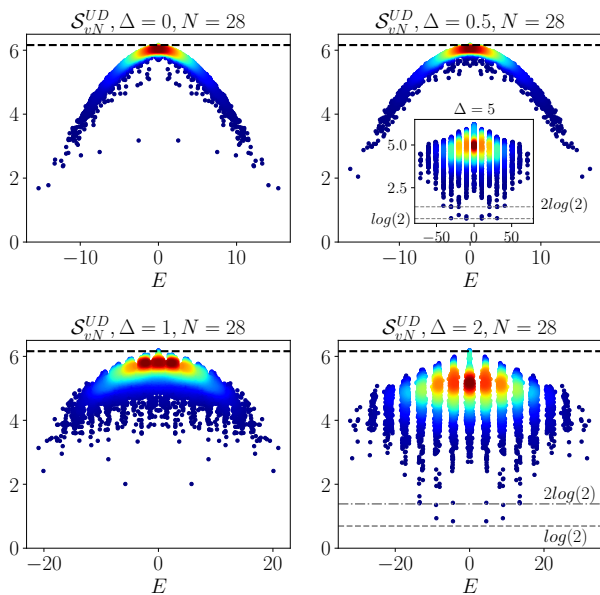


FIG. 10. Bipartite von Neumann entanglement entropy (for definition see Appendix B) of all many-body eigenstates of the Hamiltonian with respect to the UD partition at $\Delta/\Omega = 0$ (top left panel), $\Delta/\Omega = 0.5$ (top right panel), $\Delta/\Omega = 1$ (bottom left panel) and $\Delta/\Omega = 2$ (bottom right panel) respectively for $N = 28$ atoms in the $k_x = k_y = 0$ sector. The solid dashed black line denotes the Page value (i.e. the average entanglement entropy of Haar-random states) in this specific symmetry sector. The broad distribution of the values of the von Neumann entanglement entropy for $\Delta/\Omega = 1, 2$ suggest that there is a Krylov fracture of the Hilbert space, albeit approximate. Inset of the figure in top right panel is the bipartite von Neumann entanglement entropy of all many-body eigenstates of the Hamiltonian with respect to UD partition at $\Delta/\Omega = 5$, black dashed line indicates the entanglement entropy obtained from the analytical construction of the eigenstates from $\mathcal{H}_{\text{eff}}^{[2]}$ for states having 1 and 2 Bell pairs respectively which are cut by the UD partition giving a contribution of $\log 2$ per Bell pair in the entanglement entropy (see Appendix-C1).

illustrated that for all the parameter regimes discussed in the paper, the idealized kinetically constrained system (1) is overall quantum chaotic, even if various forms of ergodicity breaking behavior exists for finite-size systems at finite times for specific initial states.

IV. FLOQUET ENGINEERING

In Ref. [21], it was shown that by leveraging the underlying chirality operator associated with the PXP model (on any bipartite lattice), it is possible to design Floquet protocols, such as periodic kicks in the form of a many-body π -pulse, leading to dynamical signatures reminiscent of discrete time-crystalline (DTC) order which are stabilized by QMBS. This naturally raises the question of whether it is possible to design interesting Floquet pro-

ocols with the help of the two chirality operators $\hat{\mathcal{C}}_{1,2}$ we introduced earlier in Sec. II (see Eqs. (2),(3)). As expected, the protocol proposed in [21] (see Eq. (8)), henceforth referred to as protocol-0, gives rise to a subharmonic response (in the form of period-2 exact revivals) in the model (1) for $\Delta = 0$, starting from *any* initial state

$$\hat{U}_F(\tau) = \hat{\mathcal{C}} e^{-i\tau\hat{\mathcal{H}}_{\Delta=0}} \quad (8)$$

This happens as $\{\hat{\mathcal{H}}_{\Delta=0}, \hat{\mathcal{C}}\} = 0$ and $\hat{\mathcal{C}}^2 = \hat{\mathbb{1}}$ which implies that $\hat{U}_F^2(\tau) = \hat{\mathbb{1}}$. However, protocol-0 does not give rise to exact revivals for $\Delta \neq 0$, since $\{\hat{\mathcal{H}}_{\Delta \neq 0}, \hat{\mathcal{C}}\} \neq 0$. In what follows, we shall show that by using the appropriate chirality operators for non-zero staggered detunings, i.e. $\hat{\mathcal{C}}_{1,2}$ (Eqs. (2),(3)), we can generate two new classes of Floquet protocols, which allow us to realize exact revivals, for any $\Delta \neq 0$.

A. Protocol-I: Subharmonic response

We now consider a modified version of protocol-0, which is obtained by replacing $\hat{\mathcal{C}}$ by $\hat{\mathcal{C}}_1$ in Eq. (8), giving rise to a new protocol (henceforth referred to as protocol-I) defined by the following unitary evolution operator

$$\hat{U}_F^I(\tau) = \hat{\mathcal{C}}_1 e^{-i\hat{\mathcal{H}}\tau} \quad (9)$$

In the context of Rydberg atom quantum simulators, such a protocol can be thought of as a unitary evolution via the Hamiltonian $\hat{\mathcal{H}}$ for time τ , followed by the action of the chirality operator $\hat{\mathcal{C}}_1 = \hat{\mathcal{T}}_x \hat{\mathcal{C}}$, which itself is composed of the (instantaneous) action of a many-body π -pulse, followed by an (instantaneous) spatial translation of the atoms by one sites along the longer direction in a cyclic fashion. Successive action of this unitary on any initial state of the system, defines for us a Floquet protocol, with $\hat{U}_F^I(\tau)$ as the Floquet unitary with time period τ . For such a protocol, using Eq. (4) given earlier, one can see that $\hat{U}_F^I(2m\tau) = (\hat{U}_F^I(\tau))^{2m} = \hat{\mathcal{T}}_x^{2m}$ ($m \geq 1$). This relation implies that if an initial state $|\psi(0)\rangle$, satisfies $\hat{\mathcal{T}}_x^{2m} |\psi(0)\rangle = |\psi(0)\rangle$, then it revives exactly after $2m$ cycles under the Floquet protocol (9). In other words, *every* Fock state returns to itself exactly after a specific number of cycles, which is set by the lattice-translation properties of that state with respect to $\hat{\mathcal{T}}_x$. As a result of this delayed exact revivals, the interacting quantum many-body system described above, exhibits a state-dependent subharmonic response which is suggestive of discrete-time-crystalline order [31, 32]. This state-dependent exact revivals are illustrated in Fig. 11 by studying (numerically) the micromotion associated with protocol-I.

As mentioned earlier, implementing the protocol-I described above in real platforms, requires the technological ability to apply a many-body π -pulse and to

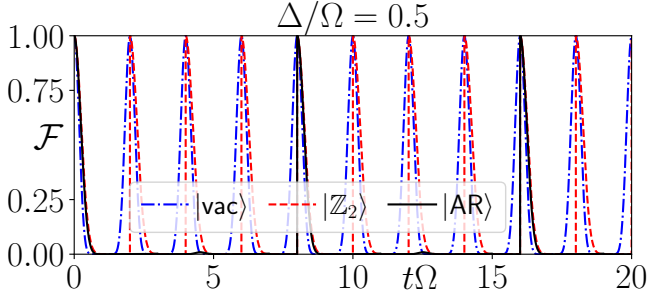


FIG. 11. Illustration of realization of exact revivals under protocol-I (Eq. (9)). Return probability $\mathcal{F}(t) = |\langle \psi(0) | \psi(t) \rangle|^2$ is plotted as a function of time starting from different initial states: (i) $|\text{vac}\rangle$ (blue dashed), (ii) $|\mathbb{Z}_2\rangle$ (red dashed) and (iii) a generic Fock state $|\text{AR}\rangle \equiv |\bullet\circ\circ\circ\bullet\circ\circ\bullet\circ\circ\rangle$ (black solid) at $\Delta = 0.5\Omega$ for $N = 16$ atoms. As evident from the figure, all states revive after a number of cycles dictated by the translational properties of the initial state. In all cases the states have been evolved using a discrete time-step integrator [29].

simultaneously (i.e. without acquiring any kinematical phase) translate the atoms to a new location. Although this is extremely challenging, in light of recently demonstrated technological progress in [7, 33], such operations may become achievable in near future.

We will now focus on how the imperfections in the action of the many-body π -pulse can influence the sub-harmonic response shown in Fig. 11. We consider the influence of an imperfect many-body π -pulse, where the phase rotation can deviate from π by an amount ϵ . In this case, the unitary evolution operator of one cycle for protocol-I becomes.

$$\hat{U}_F^I(\tau; \epsilon) = \hat{T}_x e^{-i(\pi-\epsilon)\hat{N}} e^{-i\tau\hat{H}} \quad (10)$$

where $\hat{N} = \sum_{j=1}^L \sum_{a=1}^2 \hat{n}_{j,a}$, $\hat{n}_{j,a} = (\hat{\sigma}_{j,a}^z + 1)/2$. In Fig. 12, we show the stability of the exact revivals starting from the initial state $|\text{vac}\rangle$ (top panel), $|\mathbb{Z}_2\rangle$ (middle panel) and $|\text{AR}\rangle \equiv |\bullet\circ\circ\circ\bullet\circ\circ\bullet\circ\circ\rangle$ (bottom panel) for $\Delta = 0.5, \tau = 1$ for $N = 16$ atoms at different values of ϵ , $\epsilon = 0$ (red), $\epsilon = 0.01$ (blue), $\epsilon = 0.02$ (green), $\epsilon = 0.08$ (brown) and $\epsilon = 0.1$ (black).

As the chirality operator \hat{C}_2 also anti-commutes with the Hamiltonian \hat{H} for any value of Δ , one can substitute \hat{C}_1 in Eq. (9), by \hat{C}_2 to generate an equivalent protocol that has similar features: i.e., $\hat{U}_F(2m\tau) = \hat{T}_x^{2m} \hat{T}_y^{2m}$ ($m \geq 1$). In this case, the revival period depends on the translation properties of the initial state along both directions. This can again be observed by computing the Floquet micro-motion in a similar fashion as above.

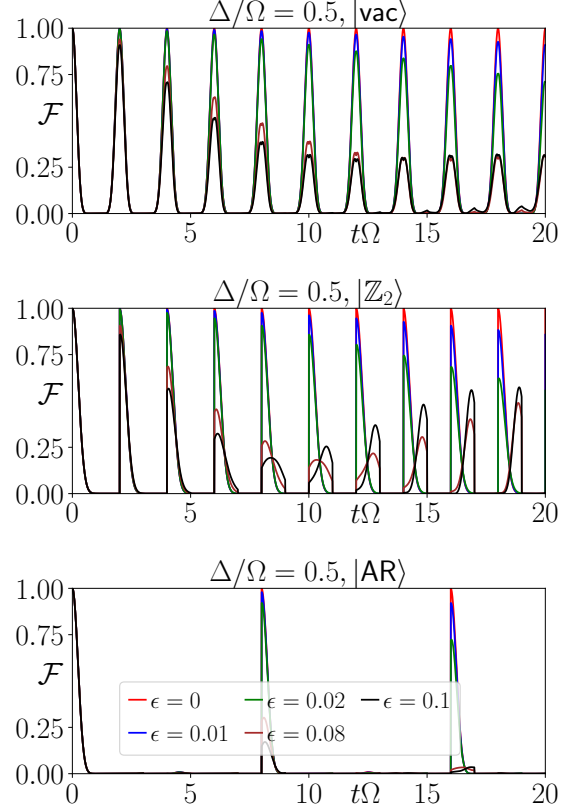


FIG. 12. This figure represents the degree of robustness of exact revivals under protocol-I due to imperfections in the many-body π -pulse. Return probability $\mathcal{F}(t) = |\langle \psi(0) | \psi(t) \rangle|^2$ is plotted as a function of time for $\Delta = 0.5, \tau = 1$ with $N = 16$ atoms starting from the states $|\text{vac}\rangle$ (top panel) and $|\mathbb{Z}_2\rangle$ (middle panel) and $|\text{AR}\rangle \equiv |\bullet\circ\circ\circ\bullet\circ\circ\bullet\circ\circ\rangle$ (bottom panel) at different values of imperfection ϵ in the π -pulse, denoted as, $\epsilon = 0$ (red), $\epsilon = 0.01$ (blue), $\epsilon = 0.02$ (green), $\epsilon = 0.08$ (brown) and $\epsilon = 0.1$ (black) respectively. As the figure illustrates, the $|\text{vac}\rangle$ state is more stable against imperfections in the application of the exact many-body π -pulse. In all cases the states have been evolved using a discrete time-step integrator [29].

B. Protocol-II: Exact Floquet flat bands

We now introduce a second class of Floquet protocol (henceforth called protocol-II), which gives rise to exact revivals after every cycle, starting from any initial state for any value of $\Delta \neq 0$ and hence constitutes a different class of dynamical phenomena compared to protocol-I. The one-cycle Floquet unitary for protocol-II reads

$$\hat{U}_F^{\text{II}}(\tau) = \hat{C} e^{-i\hat{H}_{-\Delta_0}\tau/2} \hat{C} e^{-i\hat{H}_{\Delta_0}\tau/2} \quad (11)$$

Where $\hat{H}_{\pm\Delta_0}$ is the Hamiltonian with staggered detuning $\Delta_{j,a} = (-1)^j \Delta_0$ and $\Delta_{j,a} = -(-1)^j \Delta_0$ respectively. Due to the identity

$$\hat{C} e^{-i\hat{H}_{-\Delta_0}\tau/2} \hat{C} = e^{+i\hat{H}_{\Delta_0}\tau/2} \quad (12)$$

We have

$$\hat{U}_F^{\text{II}}(\tau) = \hat{C} e^{-i\hat{H}_{-\Delta_0}\tau/2} \hat{C} e^{-i\hat{H}_{+\Delta_0}\tau/2} = \hat{1} \quad (13)$$

$$\begin{aligned} & \hat{C} \frac{(-i\tau/2)^m}{m!} \overbrace{(\hat{H}_z + \hat{H}_x) \dots (\hat{H}_z + \hat{H}_x) \dots (\hat{H}_z + \hat{H}_x)}^{m \text{ terms}} \hat{C} \\ &= \frac{(-i\tau)^m}{2^m m!} \overbrace{\hat{C}^{-1} (\hat{H}_z + \hat{H}_x) \hat{C} \dots \hat{C}^{-1} (\hat{H}_z + \hat{H}_x) \hat{C} \dots \hat{C}^{-1} (\hat{H}_z + \hat{H}_x) \hat{C}}^{m \text{ terms}} \\ &= \frac{(-i\tau)^m}{2^m m!} \overbrace{(\hat{H}_z - \hat{H}_x) \dots (\hat{H}_z - \hat{H}_x) \dots (\hat{H}_z - \hat{H}_x)}^{m \text{ terms}} \\ &= \frac{(-i\tau)^m}{2^m m!} (-1)^m \overbrace{(-\hat{H}_z + \hat{H}_x) \dots (-\hat{H}_z + \hat{H}_x) \dots (-\hat{H}_z + \hat{H}_x)}^{m \text{ terms}} = \frac{(+i\tau)^m}{2^m m!} \hat{H}_{-\Delta_0} \end{aligned} \quad (14)$$

In the manipulations above, we have used the following two equations, which follow from the algebra of the Pauli spin operators.

$$\hat{C}^{-1} \hat{H}_z \hat{C} = +\hat{H}_z \quad (15a)$$

$$\hat{C}^{-1} \hat{H}_x \hat{C} = -\hat{H}_x \quad (15b)$$

As we can see from Eq. (14), the term corresponding to the m -th power of τ in the LHS of Eq. (12) is equal to the m -th power of Eq. (12) in the RHS, which implies that the identity Eq. (12) holds. This in turn completes the proof that for drive protocol Eq. (11), $\hat{U}_F^{\text{II}}(\tau) = \hat{1}$.

Since $\hat{U}_F^{\text{II}}(\tau) = \hat{1}$, under protocol-II, every initial state exhibits exact revivals with a period equal to the time period of the protocol (τ) and the system hosts exact Floquet flat bands at any value of $\Delta_0 \neq 0$. This is illustrated in Fig. 13 by studying (numerically) the micro-motion associated with the protocol-II for a system with $N = 20$ atoms, $\Delta_0 = 0.5$, $\tau = 1$ for three different initial states (same as those in Fig. 11).

Similar to the case of protocol-I, We will now return to the question of how the imperfections in the action of the many-body π -pulse influences the appearance of exact Floquet flat band as depicted in Fig. 13.

As mentioned in the above section, we consider an imperfect many-body π -pulse, where the deviation in the phase rotation from π is symbolically represented by an amount ϵ . In this case, the one-cycle unitary takes the following form

$$\hat{U}_F^{\text{II}}(\tau; \epsilon) = e^{-i(\pi-\epsilon)\hat{N}} e^{-i\hat{H}_{-\Delta_0}\tau/2} e^{-i(\pi-\epsilon)\hat{N}} e^{-i\hat{H}_{\Delta_0}\tau/2} \quad (16)$$

The validity of the identity Eq. (12) can be verified by expanding the exponential on it's left hand side (LHS) in powers of τ and showing that it is equal to the corresponding term in the right hand side (RHS). This equivalence for the m^{th} power is shown below

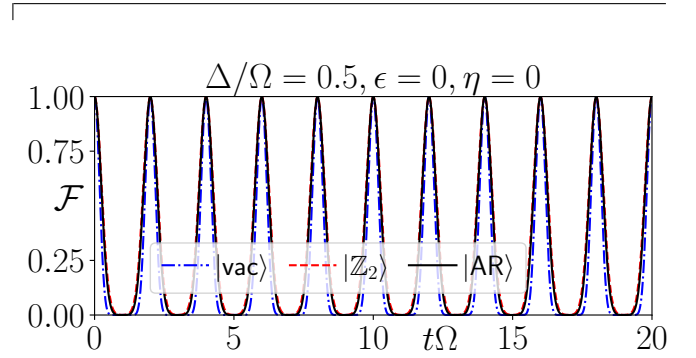


FIG. 13. Illustration of realization of exact Floquet flat band via protocol-II starting from different initial states. Return probability $\mathcal{F}(t) = |\langle \psi(0) | \psi(t) \rangle|^2$ is plotted as a function of time starting (i) $|\text{vac}\rangle$ (blue dashed line), (ii) $|\mathbb{Z}_2\rangle$ (red dashed line) and (iii) a generic Fock state $|\text{AR}\rangle = |\bullet\bullet\bullet\bullet\bullet\bullet\bullet\bullet\bullet\bullet\bullet\bullet\bullet\bullet\bullet\bullet\rangle$ (black dashed line) at $\Delta_0 = 0.5\Omega$ for $N = 16$ atoms. As evident from the figure, all states revive after exactly one cycle of the protocol described in Eq. (11). In all cases the states have been evolved using a discrete time-step integrator [29].

where $\hat{N} = \sum_{j=1}^L \sum_{a=1}^2 \hat{n}_{j,a}$, $\hat{n}_{j,a} = (\hat{\sigma}_{j,a}^z + 1)/2$. In Fig. 14, we show the nature of the revivals starting from the initial state $|\text{vac}\rangle$ (top panel), $|\mathbb{Z}_2\rangle$ (middle panel) and $|\text{AR}\rangle \equiv |\bullet\bullet\bullet\bullet\bullet\bullet\bullet\bullet\bullet\bullet\bullet\bullet\bullet\bullet\bullet\bullet\rangle$ (bottom panel) for $\Delta_0 = 0.5$, $\tau = 1$ for $N = 16$ atoms at different values of ϵ , $\epsilon = 0$ (red), $\epsilon = 0.01$ (blue), $\epsilon = 0.02$ (green), $\epsilon = 0.08$ (brown) and $\epsilon = 0.1$ (black).

Figs. 12,14 indicate that the Rydberg vacuum state (see top panels of Figs. 12,14) is more stable against the imperfection in the application of the many-body π -pulse for both the protocol-I and protocol-II. We have not been able to understand the reason of such stability and a detailed analysis of this reason will be a subject of future study.

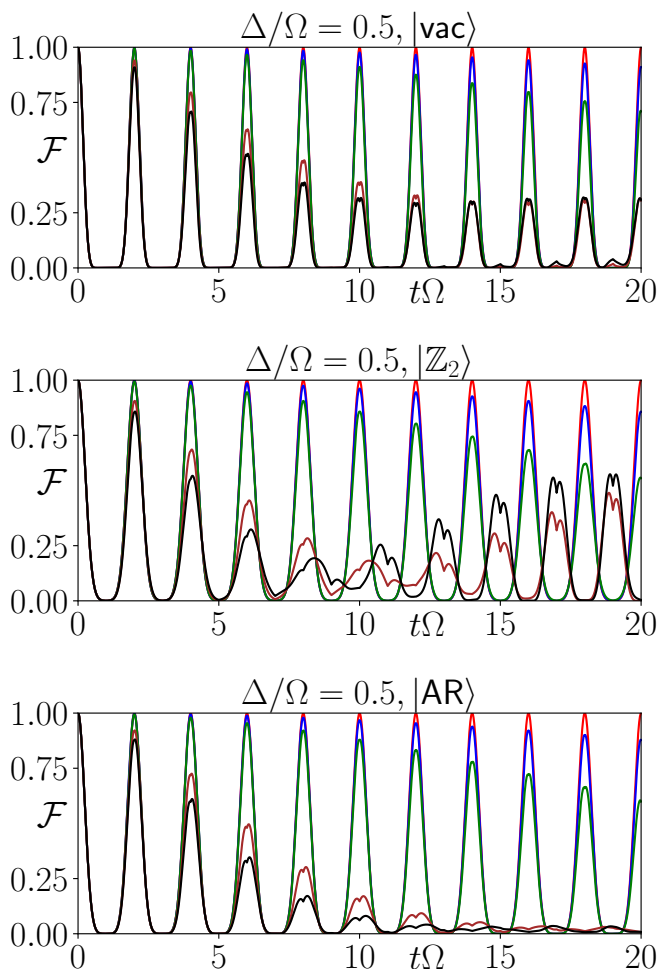


FIG. 14. This figure demonstrates the robustness of exact revivals under protocol-II due to imperfections in the many-body π -pulse. In this figure the return probability $\mathcal{F}(t) = |\langle \psi(0) | \psi(t) \rangle|^2$ is plotted as a function of time starting for $\Delta_0 = 0.5\Omega$, $\tau = 1$ with $N = 16$ atoms starting from the states $|\text{vac}\rangle$ (top panel) and $|\mathbb{Z}_2\rangle$ (middle panel) and $|\text{AR}\rangle \equiv |\bullet\circ\circ\circ\bullet\circ\circ\bullet\circ\circ\bullet\circ\circ\rangle$ (bottom panel) at different values of imperfection ϵ in the π -pulse, denoted as, $\epsilon = 0$ (red), $\epsilon = 0.01$ (blue), $\epsilon = 0.02$ (green), $\epsilon = 0.08$ (brown) and $\epsilon = 0.1$ (black) respectively. In all cases the states have been evolved using a discrete time-step integrator [29].

V. EFFECTS OF ENVIRONMENT

The relevant experimental platforms, which host such model Hamiltonians, i.e., Rydberg atom quantum simulator platforms, have inevitable interactions with the environmental degrees of freedom [1, 34]. In a real system, the Rydberg excited states have a finite lifetime and it might be possible that the Rydberg excited state of an atom undergoes spontaneous emissions, which projects it onto the Rydberg ground-state of that atom from time to time. For a single atom in such a platform, an incoherent dynamics may appear as a

result of fluctuations in the Rabi frequency and the detunings from one shot to another in a real experiment. These environmental effects at a single atom level can accumulate in an interacting many-body setup and give rise to interesting dynamics that cannot be explained by considering only unitary evolution governed by a Hamiltonian. Thus, it would be important to check the robustness of the emergent conservation laws and of the quantum many-body scars when such environmental loss channels are present. There are also other effects that could appear due to lattice imperfections and can be handled by considering a quenched disorder in the couplings of the Hamiltonian while still considering the system as being isolated and evolving unitarily.

In this section, we focus on studying the effect of the inevitable coupling to an external environment on the nature of the anomalous non-equilibrium dynamics discussed in Sec. III. In this paper we will only study the effects of two such environmental loss channels: (i) pure dephasing and (ii) spontaneous emission of photons due to the finite lifetime of Rydberg excited states. Both of these effects have been addressed by considering the Lindblad master equation as a description of the quantum dynamics of this open quantum system. This Lindblad master equation is an equation of motion for the full density matrix of the system, which describes both coherent and dissipative parts of the evolution within the paradigm of Born-Markov approximation. The dissipative part of the quantum dynamics arising due to the aforementioned loss channels are manifested by the action of appropriate jump-operators $\hat{J}_{\{\alpha\}}$ associated with the loss channels $\{\alpha\}$. For pure dephasing, these jump-operators take the form $\hat{J}_{j,a}^{(d)} = \sqrt{\gamma_d} \hat{\sigma}_{j,a}^z$ while for spontaneous emission $\hat{J}_{j,a}^{(e)} = \sqrt{\gamma_e} \hat{\sigma}_{j,a}^-$, where γ_d and γ_e denote the strength of the dephasing and decay rate of the Rydberg excited-state respectively.

Within the Born-Markov approximation [34], the full open quantum dynamics of a many-body quantum system (in terms of its density operator $\hat{\rho}(t)$) is governed by the Gorini-Kossakowski-Sudarshan-Lindblad (GKSL) master equation, which is often referred to as simply the Lindblad master equation. This master equation has the following form

$$\begin{aligned} \frac{d\hat{\rho}(t)}{dt} &= \hat{\mathcal{L}}[\hat{\rho}(t)] \\ &= -i[\hat{\mathcal{H}}, \hat{\rho}(t)] + \sum_{\alpha} \left(\hat{J}_{(\alpha)} \hat{\rho}(t) \hat{J}_{(\alpha)}^{\dagger} - \frac{1}{2} \left\{ \hat{J}_{(\alpha)}^{\dagger} \hat{J}_{(\alpha)}, \hat{\rho}(t) \right\} \right) \end{aligned} \quad (19)$$

Where \sum_{α} symbolically denotes the sum over all quantum channels described by the jump operators $\hat{J}_{(\alpha)}$. In these subsequent sections, we will focus on (i) fate of the quantum many-body scar induced persistent oscillations observed in [24] and (ii) robustness of the emergent approximate conservation laws (see Sec. III B of main text

and Appendix-C) that appear in the limit ($\Delta/\Omega \gg 1$) when the two aforementioned environmental loss channels are considered.

A. Stability of QMBS

1. Dephasing

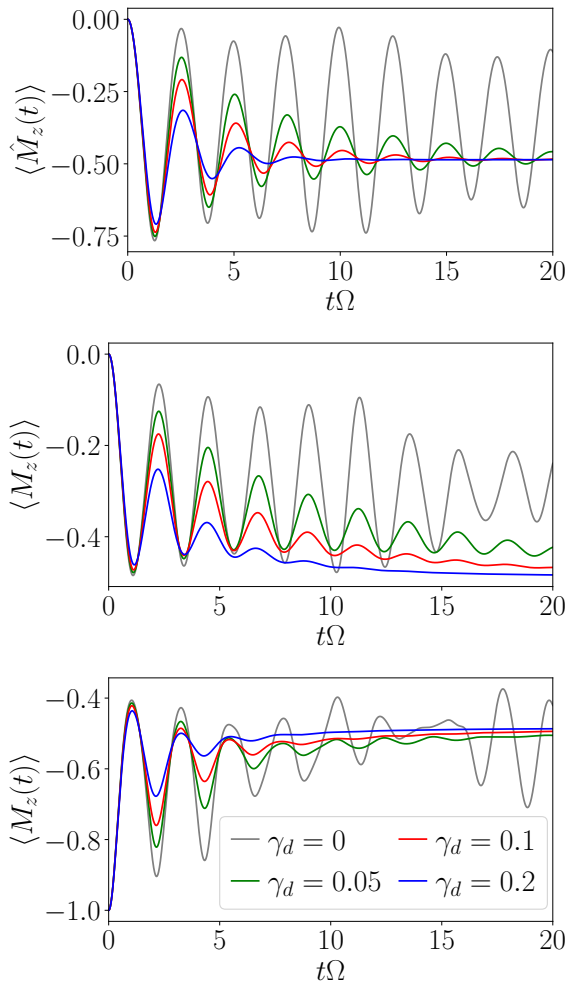


FIG. 15. Evolution of $\langle \hat{M}_z(t) \rangle$ as a function of time t for (i) $\Delta = 0, |\psi(0)\rangle = |\mathbb{Z}_2\rangle$, (ii) $\Delta = 1, |\psi(0)\rangle = |\mathbb{Z}_2\rangle$ and (iii) $\Delta = 1, |\psi(0)\rangle = |\text{vac}\rangle$, considering that the Rydberg atoms experience dephasing at a rate $\gamma_d/\Omega = 0, 0.05, 0.1, 0.2$

In Fig. 15, we show the evolution of average magnetization $\langle \hat{M}_z(t) \rangle \equiv \text{Tr}[\hat{\rho}(t)\hat{M}_z]$, where $\hat{\rho}(t)$ is the instantaneous (normalized) density operator of the system governed by Eq. (17) and $\hat{M}_z \equiv \sum_{j=1}^L \sum_{a=1}^2 \hat{\sigma}_{j,a}^z/N$. We consider three different combinations of the staggered detuning strength (Δ) and initial pure state ($|\psi(0)\rangle$): (i) $\Delta = 0, |\psi(0)\rangle = |\mathbb{Z}_2\rangle$, (ii) $\Delta = 1, |\psi(0)\rangle = |\mathbb{Z}_2\rangle$ and (iii) $\Delta = 1, |\psi(0)\rangle = |\text{vac}\rangle$ in the presence of a non-zero dephasing γ_d . At these parameter points, the chosen states

exhibit persistent oscillations due to presence of QMBS [24] in the closed system undergoing unitary evolution. However, our results indicate that these persistent oscillations are not robust against dephasing: an increase in the dephasing rate diminishes the off-diagonal components of the density matrix (in Fock basis), resulting in the loss of coherent oscillations. In this steady-state ($d\hat{\rho}/dt = 0$) all the Fock states have the same weight, which combined with the constrained nature of the Hilbert space of the system governed by Eq. 1, implies that the steady-state magnetization value is close to $-1/2$ in the presence of any non-zero dephasing, as evident from the Fig. 15. This figure also demonstrates that for very weak dephasing strengths e.g., $\gamma_d/\Omega = 0.05$, the persistent oscillations in average magnetization evolution do still appear in the same frequency of oscillation as observed for unitary evolution, albeit with a reduced amplitude.

2. Spontaneous emission

In Fig. 16, we show the evolution of average magnetization $\langle \hat{M}_z(t) \rangle$ as a function of time t , for (i) $\Delta = 0, |\psi(0)\rangle = |\mathbb{Z}_2\rangle$, (ii) $\Delta = 1, |\psi(0)\rangle = |\mathbb{Z}_2\rangle$ and (iii) $\Delta = 1, |\psi(0)\rangle = |\text{vac}\rangle$ considering that an atom in the Rydberg-excited state can spontaneously emit a photon at rate γ_e and relax to the Rydberg ground-state. As mentioned in the previous sections, for these parameter choices the isolated system ($\gamma_e = 0$) exhibits persistent oscillations due to presence of QMBS (also see [24]). For a non-zero spontaneous emission rate, there is a competition between the Rabi spin-flip term and the spontaneous emission term: if no spin-flip processes occur, then the system in the presence of spontaneous emissions, will continuously convert all the Rydberg-excited atoms into Rydberg ground-state atoms and the final steady-state will be the Rydberg vacuum state $|\text{vac}\rangle$. Thus, the steady-state expectation value of the average magnetization operator, \hat{M}_z would be -1 , and $\langle \hat{M}_z(t) \rangle$ would approach this value as time evolves, with the rate of approaching the steady-state being proportional to γ_e . When there are spin-flip processes induced by the Rabi oscillation term in the Hamiltonian, there will be competition between the strength of coherent oscillation in the constrained Hilbert space i.e. the Rabi frequency 2Ω and the strength of spontaneous emission γ_e . As a result, the steady-state magnetization value will depend on the specific choice of the parameter values used in the Lindblad evolution. For $\Omega \gg \gamma_e$, the steady-state magnetization (M_z^{ss}) value would approach $-1/2$, i.e., $M_z^{\text{ss}} \sim -1/2$ (see top panel of Fig. 16) following the arguments given in Sec. V A 1, whereas in the opposite regime, i.e., $\Omega \ll \gamma_e$ one has $M_z^{\text{ss}} \sim -1$. In the intermediate regimes, the value of M_z^{ss} has to be computed explicitly by solving the equation of the steady-state $d\hat{\rho}/dt = 0$. In Fig. 16 we show the evolution of average magnetization $\langle \hat{M}_z(t) \rangle$ as a function of time t , for the aforementioned three different combinations of $\Delta, |\psi(0)\rangle$ at four representative values of

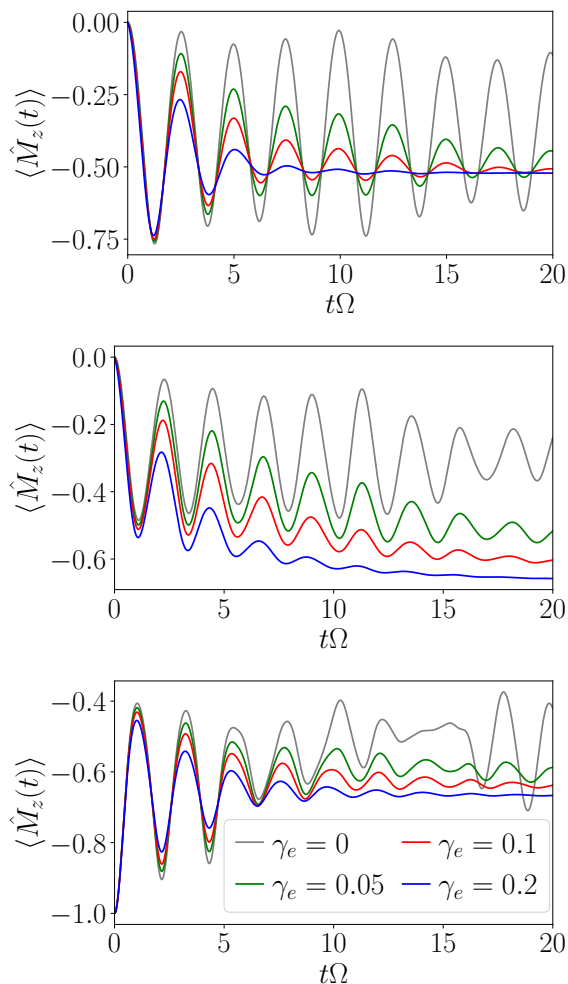


FIG. 16. Evolution of $\langle \hat{M}_z(t) \rangle$ as a function of time t for (i) $\Delta = 0, |\psi(0)\rangle = |\mathbb{Z}_2\rangle$, (ii) $\Delta/\Omega = 1, |\psi(0)\rangle = |\mathbb{Z}_2\rangle$ and (iii) $\Delta = 1, |\psi(0)\rangle = |\text{vac}\rangle$, considering that the Rydberg excited state can spontaneously emit a photon with rate rate $\gamma_e = 0$ (gray solid line), $\gamma_e = 0.05$ (green solid line), $\gamma_e = 0.1$ (red solid line), and $\gamma_e = 0.2$ (blue solid line) respectively. See text for details.

the decay rate $\gamma_e = 0$ (gray solid line), $\gamma_e = 0.05$ (green solid line), $\gamma_e = 0.1$ (red solid line), and $\gamma_e = 0.2$ (blue solid line) respectively, for a ladder with $N = 8$ atoms. The figures demonstrate that the persistent oscillations observed in the unitary evolution, are not robust against spontaneous emission for generic initial states. However, as observed in the bottom panel of Fig. 16, for the state $|\psi(0)\rangle = |\text{vac}\rangle$, consisting of all atoms in the Rydberg ground-state, the persistent oscillations in the magnetization dynamics are more robust against spontaneous emission.

B. Stability of Approximate Emergent Conservation Laws

We now consider the behavior of the quasi-conserved charge $\langle \hat{Q}_1(t) \rangle \equiv \text{Tr}[\hat{\rho}(t)\hat{Q}_1]$ under the time evolution governed by the Lindblad master equation (see Eq. (17)). In Fig. 17 we consider three initial states, namely (i) $|\psi_0\rangle = |\mathbb{Z}_2\rangle$ (top panel), (ii) $|\psi_0\rangle = |1P\rangle$ (middle panel) and (iii) $|\psi_0\rangle = |\text{vac}\rangle$ (bottom panel) for a 2-leg ladder with $N = 8$ atoms at $\Delta = 4\Omega$ and different strengths of environmental loss channels: $\gamma_d/\Omega = 0.1$ (red solid curve), $\gamma_d/\Omega = 0.2$ (blue solid curve), $\gamma_e/\Omega = 0.1$ (red dashed curve), $\gamma_e/\Omega = 0.2$ (blue dashed curve), $\gamma_d = \gamma_e = 0$ (gray solid curve). This figure exhibits the robustness of the conservation laws against the two aforementioned loss channels.

It is expected and also evident from Fig. 17 that for generic initial states, the emergent conservation laws are more stable against dephasing than compared to spontaneous emission, since one event of spontaneous emission of Rydberg-excited atoms on any of the sites $(j, 1)$ or $(j, 2)$ changes the sign of the quasi-conserved charge \hat{Q}_j . Furthermore, we note that pure dephasing does not alter the sign of the quasi-conserved charge $\langle \hat{Q}_1(t) \rangle$ for all the initial states considered here up to times $t\Omega \sim 20$. Hence, the storage of $L/2$ classical bits of information by the utilization of sign of such emergent approximate conservation laws as discussed in Appendix-C 2 is a robust mechanism even in the presence of pure-dephasing. There is an important exception to this generic expectation: there exists one special initial state, namely the $|\text{vac}\rangle$ state, for which the quasi-conserved charges seem to be more robust against spontaneous emission compared to dephasing. From the inset of the bottom panel of Fig. 17 it becomes evident that for the $|\text{vac}\rangle$ state, an increased strength of the rate of spontaneous emission (γ_e) enhances the degree of fulfillment of the approximate emergent conservation laws. This happens as after each event of spontaneous emission, one Rydberg excited-atom is converted into a Rydberg ground-state and hence the expectation value of the quasi-conserved charges shift towards the initial time expectation value with respect to the $|\text{vac}\rangle$ state.

Individual Quantum Trajectories: The evolution of the Lindblad master equation describes the non-unitary evolution of the system's density matrix within the Born-Markov approximation [34]. This non-unitary nature of the dynamics arises from the fact that the system is interacting with the environment which results in incoherent evolution of the system's degrees of freedom. It is possible to describe the solution of the GKSL master equation as an average over the ensemble of density matrices constructed from several realizations of stochastically evolved pure quantum states where the stochasticity comes from the continuous monitoring of the quantum system under consideration. This completely equivalent

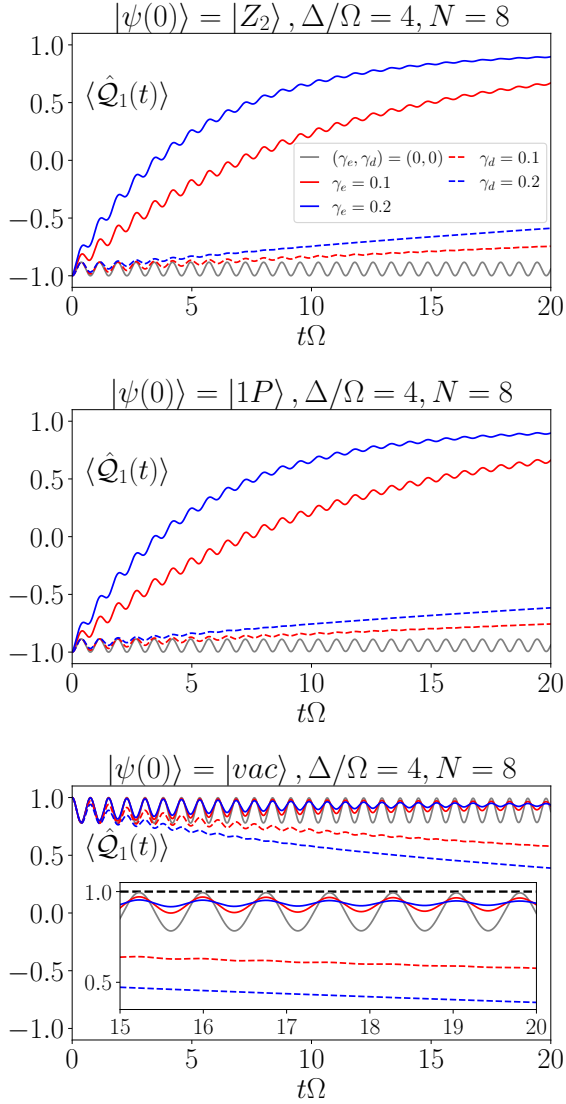


FIG. 17. Illustration of the stability of the emergent quasi-conserved charges \hat{Q}_1 at $\Delta/\Omega = 4$ starting from three different initial states ($|Z_2\rangle$ top panel, $|1P\rangle$ middle panel and $|vac\rangle$ bottom panel) under dephasing ($\gamma_d \neq 0$) and spontaneous emission ($\gamma_e \neq 0$) for a 2-leg ladder with $N = 8$ atoms. Different colors in the figure indicate different values of the strength of the rate of dephasing and spontaneous emission with $\gamma_e, \gamma_d = (0, 0)$ (gray solid line), $\gamma_e = 0.1$ (red solid line), $\gamma_e = 0.2$ (blue solid line), $\gamma_d = 0.1$ (red dashed line) and $\gamma_d = 0.2$ (blue dashed line) respectively. In all the figures, the colors are the same as that of the top panel. See text for details.

approach known as Monte Carlo wave function (MCWF) approach, or as the quantum trajectory approach, allows one to track the evolution of the open system as a function of time in terms of pure quantum states [34–38]. In the quantum trajectory approach, one evolves the quantum state $|\psi(t)\rangle$, which is a vector of dimension \mathcal{D}_H (\mathcal{D}_H being the Hilbert space dimension) and is thus computa-

tionally less expensive than the full Lindblad evolution. Apart from the lower numerical complexity, analysis of individual quantum trajectories are also important due to the fact that when a physical noisy quantum hardware under continuous monitoring evolves in time, it does not evolve according to the Lindblad evolution, but rather follows a stochastic pure state evolution which is similar to a single realization of a quantum trajectory, where the jumps ($\hat{J}_{(\alpha)}$) correspond to a manifestation of a physical loss in the system [39]. The quantum trajectory approach also enables the possibility of monitoring quantum entanglement of the system under different continuous measurement processes [40, 41].

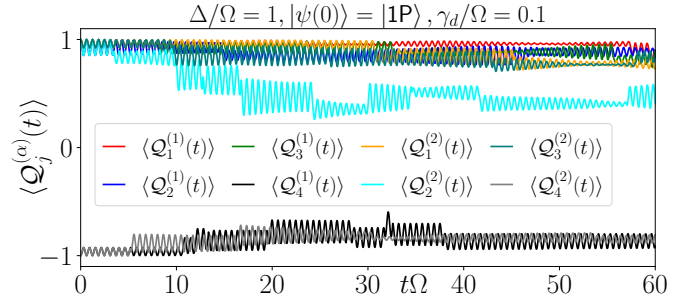


FIG. 18. Time evolution of the instantaneous expectation values of the approximate emergent conserved charges $\hat{Q}_j^{(\alpha)}$ ($j = 1, 2, 3, 4$ stands for rung index in a 2-leg square ladder with $N = 8$ atoms) starting from the $|1P\rangle \equiv |\circ\circ\circ\circ\rangle$ state at $\Delta/\Omega = 5$, for two different quantum trajectories $\alpha = 1, 2$ when dephasing ($\gamma_d = 0.1\Omega$) is considered. This figure shows that the sign of conserved charges do not alter during the evolution for two different realization of the quantum trajectory MCWF method. This is the case for most of the trajectories as the average Lindblad description also depicts the same scenario. See Fig. 17 and text for details.

As shown in Fig. 17, the emergent approximation laws, when starting from a generic initial state, seem to be more robust against dephasing loss mechanism compared to spontaneous emissions. For this reason, it is interesting to look at individual quantum trajectories for the dephasing case. In Fig. 18 we show evolution of all the approximately conserved charges starting from the $|1P\rangle$ state, when a dephasing rate $\gamma_d = 0.1\Omega$ is considered. This figure illustrates that even for individual quantum trajectories, the conservation laws seem to be respected approximately. Moreover, the sign of the conserved charges do not change in time for a long duration, which further strengthens the classical bit storage capabilities illustrated in Appendix-C 2

VI. CONCLUSION AND OUTLOOK

In this paper we have demonstrated that leveraging the controllability of Rydberg atom platforms in terms of both the geometry of the optical tweezer arrays as well as

the tunability of the external parameters, enables us to realize various forms of anomalous quantum dynamics: (i) appearance of extensive number of emergent conservation laws leading to approximate Krylov fractures and integrability-induced slow dynamics, (ii) Floquet protocols leading to subharmonic responses reminiscent of discrete-time-crystalline order and exact Floquet flat bands. We have also presented a basic analysis of the stability of some of the dynamical features against imperfections of various kinds namely, imperfections in the application of a many-body π -pulse and effects of environmental loss channels such as spontaneous emission and dephasing. Our results indicate that the Rydberg vacuum state is more stable against imperfections in the application of a many-body π -pulse for both protocol-I and protocol-II. We have not been able to understand the reason of such stability and a detailed analysis of this reason will be the subject of future study. We have also demonstrated that the emergent conservation laws are stable against pure-dephasing but not against the consideration of the finite lifetime of the Rydberg-excited states by looking at the evolution of the system density matrix via the Lindblad master equation. This conclusion was further supported by the robustness of the conservation laws for individual quantum trajectories. Our results indicate that both the conservation laws and the quantum many-body scars are unstable in the presence of both dephasing and spontaneous emission from the Rydberg excited states.

Finally we shown that in practice it could be challenging to implement the specific kinematical constraints illustrated in Fig. 1 in an actual Rydberg atom quantum simulator platform with only isotropic van der Waals repulsive interactions, making it difficult to observe these broad class of dynamical phenomena in an actual experimental setup. This can be attributed to the fact that for an actual Rydberg atom quantum simulator configured in the ladder geometry (Fig. 1), the strength of the second nearest-neighbor repulsive interactions, i.e. interactions among the diagonally placed atoms, are not negligible compared to the repulsive interaction energy of the first nearest neighbors. We discuss this briefly in Appendix-E. We have also pointed out that there exists an interesting parameter regime where the Néel state undergoes persistent revivals even in the full system with long-range van der Waals repulsive interactions which can be mimicked by adding next-nearest neighbor interactions in addition to Eq. (1).

However, our analysis in this paper leads us to believe that engineering of the kinematic constraints shown in Fig. 1 opens up a range of possibilities for exploring novel out-of-equilibrium phases and phenomena in real quantum hardware. In this regard, using more sophisticated orbitals such as P or D orbitals as the electronic excited states of Rydberg atoms may be useful, as they allow us take advantage of the appearance of novel “magic

distances” [42] and can aid the engineering of such kinetic constraints in Rydberg atom quantum simulator platforms. This can open up the possibility of exploiting more complex form of atomic interactions realizable in real quantum hardware, and has larger possibilities in the fields of quantum simulation, quantum information processing and quantum computation applications.

Thus in conclusion tuning the geometry [24], dimensionality [43] and trying out different atomic species [44] by utilizing their hyperfine degrees of freedom, it could be possible to design and explore a broad class of interacting quantum many-body systems with novel phases and dynamical features. This may open up a gateway towards exploring minimal models of other rich variety of interacting quantum field theories and lattice gauge theories present ubiquitously in particle physics apart from those observed in Ref. [1, 9, 45]. We would address these in our future studies related to Rydberg atom quantum simulator platforms.

VII. ACKNOWLEDGEMENTS

The authors would like to thank Arnab Sen, Immanuel Bloch, Vedika Khemani, Peter Zoller, Klaus Mølmer and Shovan Dutta for stimulating discussions and insightful comments. The authors would also like to acknowledge valuable discussions in two consecutive programs held at ICTS-TIFR – “A Hundred Years of Quantum Mechanics” (code: ICTS/qm100-2025/01) and “Quantum Trajectories” (code: ICTS/QuTr2025/01).

Appendix A: Symmetries of the Hamiltonian and Hilbert Space Dimensions

In this section, we chart out the symmetries of the model (1). By inspection we note that for $\Delta \neq 0$, the Hamiltonian commutes with the operators $\hat{\mathcal{T}}_x^2$ and $\hat{\mathcal{T}}_y$. It is possible to construct a computational basis, in which the basis states are labeled by the eigenvalues of the symmetry operators $\hat{\mathcal{T}}_x^2$ and $\hat{\mathcal{T}}_y$ (see Ref. [46] for a review on construction of symmetry reduced Hilbert spaces). For reference, in Table I, we list the Hilbert space dimensions of some chosen sectors of these symmetry operators. The eigenvalues of $\hat{\mathcal{T}}_x^2$ and $\hat{\mathcal{T}}_y$ are denoted by k_x and k_y respectively in Table-I.

It is crucial to note that the Hamiltonian (1) has additional lattice symmetries when $\Delta = 0$. In this case the Hamiltonian (1) commutes with the operators $\hat{\mathcal{T}}_x$, $\hat{\mathcal{T}}_y$ and $\hat{\mathcal{P}}_x$.

N	No Symmetry	$k_x = 0$	$k_{x,y} = 0$	$k_x = 0, k_y = \pi$	$k_{x,y} = \pi$
4	7	7	5	2	0
8	35	21	12	9	8
12	199	71	36	35	32
16	1,155	301	156	145	144
20	6,727	1,351	676	675	672
24	39,203	6,581	3,308	3,273	3,264
28	228,487	32,647	16,324	16,323	16,320
32	1,331,715	166,621	83,388	83,283	83,232

TABLE I. Hilbert space dimensions of (1) (with $\Delta \neq 0$) for system size $N = 4 - 32$ without any symmetry and for some specific symmetry sectors labeled by k_x and k_y (the eigenvalues of the symmetry operators \hat{T}_x^2 and \hat{T}_y respectively).

Appendix B: Entanglement Measures

The bipartite von Neumann entanglement entropy [47, 48] for any (pure) quantum state $|\psi\rangle$, given the bipartition $\mathcal{X}, \mathcal{X}^c$ ($\mathcal{X} \cup \mathcal{X}^c = \mathcal{E}$, the entire system), is defined as,

$$S_{\text{ent}}^{\text{vN}}(\mathcal{X}) = -\text{Tr}_{\mathcal{X}}(\rho_{\mathcal{X}} \log \rho_{\mathcal{X}}) \quad (\text{B1})$$

where $\rho_{\mathcal{X}} = \text{Tr}_{\mathcal{X}^c}(|\psi\rangle\langle\psi|)$ is the reduced density matrix (RDM) of sub-system \mathcal{X} with respect to its conjugate \mathcal{X}^c .

In the main text, we have presented results for two kinds of bi-partitions, namely (i) ‘‘LR’’ (short for left-right) partition and (ii) ‘‘UD’’ (short for up-down) partition. In the LR partition, \mathcal{X} is either taken to be left half or the right half of the ladder. For setting a fixed convention, we make this bi-partition along the middle (in the sense of site indices) of the chain. For the UD partition, \mathcal{X} is either the upper leg or the lower leg of the ladder.

For a kinetically constrained system like (1), the Hilbert space does not have a direct product structure: for any bi-partition $\mathcal{X}, \mathcal{X}^c$ with $\mathcal{X} \cup \mathcal{X}^c = \mathcal{E}$, the full Hilbert space, say $\mathcal{H}_{\mathcal{E}}$, is not equivalent to the direct product of Hilbert spaces $\mathcal{H}_{\mathcal{X}}$ and $\mathcal{H}_{\mathcal{X}^c}$ i.e., $\mathcal{H}_{\mathcal{E}} \neq \mathcal{H}_{\mathcal{X}} \otimes \mathcal{H}_{\mathcal{X}^c}$ (both Hilbert spaces $\mathcal{H}_{\mathcal{X}}$ and $\mathcal{H}_{\mathcal{X}^c}$ are obtained by considering open boundary conditions). In such a scenario, a quantum state $|\psi\rangle \in \mathcal{H}_{\mathcal{E}}$, can in principle be expressed in the product Hilbert space $\mathcal{H}_{\mathcal{X}} \otimes \mathcal{H}_{\mathcal{X}^c}$ as

$$|\psi\rangle = \sum_{\alpha=1}^{\mathcal{D}_{\mathcal{X}}} \sum_{\beta=1}^{\mathcal{D}_{\mathcal{X}^c}} \psi_{\alpha,\beta}^{\mathcal{X},\mathcal{X}^c} |\Phi_{\alpha}^{\mathcal{X}}\rangle \otimes |\Phi_{\beta}^{\mathcal{X}^c}\rangle \quad (\text{B2})$$

where $\{\psi_{\alpha,\beta}^{\mathcal{X},\mathcal{X}^c}\}$ are complex numbers describing the state, $\{|\Phi_{\alpha}^{\mathcal{X}}\rangle\}, \{|\Phi_{\beta}^{\mathcal{X}^c}\rangle\}$ are suitable basis for $\mathcal{H}_{\mathcal{X}}$ and

$\mathcal{H}_{\mathcal{X}^c}$ respectively with Hilbert space dimensions $\mathcal{D}_{\mathcal{X}}$ and $\mathcal{D}_{\mathcal{X}^c}$. The Hilbert space constraint is taken care of by the additional condition that for indices α, β , for which the state $\text{ket } |\Phi_{\alpha}^{\mathcal{X}}\rangle \otimes |\Phi_{\beta}^{\mathcal{X}^c}\rangle \notin \mathcal{H}_{\mathcal{E}}$, i.e. does not satisfy the Hilbert space constraint, we simply fix $\psi_{\alpha,\beta}^{\mathcal{X},\mathcal{X}^c} = 0$. Once the state $|\psi\rangle$ has been written in the form of Eq. (B2), one can readily compute partial traces of $|\psi\rangle\langle\psi|$ over the Hilbert space of \mathcal{X}^c to obtain the sub-system RDM $\rho_{\mathcal{X}}$, required for computing the desired entanglement entropy via Eq. (B1).

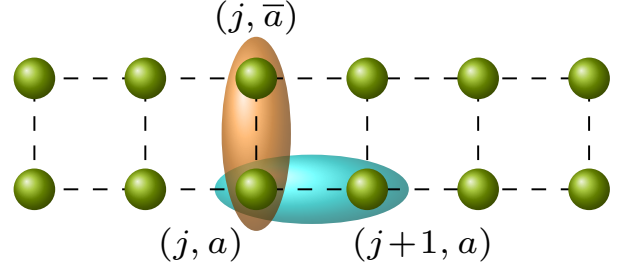


FIG. 19. Schematic illustration of the mutual information computation for the horizontal (cyan) and vertical bonds (orange). Also see Eq. (B3) and text below it.

In Sec. III B, we also considered the evolution of mutual information between two sites. In general, the mutual information between any two subsystems, \mathcal{X} and \mathcal{Y} is defined as

$$\mathcal{I}(\mathcal{X}, \mathcal{Y}) = S_{\text{ent}}^{\text{vN}}(\mathcal{X}) + S_{\text{ent}}^{\text{vN}}(\mathcal{Y}) - S_{\text{ent}}^{\text{vN}}(\mathcal{X} \cup \mathcal{Y}) \quad (\text{B3})$$

This quantity $\mathcal{I}(\mathcal{X}, \mathcal{Y})$ for any state, for any bipartition \mathcal{X}, \mathcal{Y} , describes the total amount of correlation shared between \mathcal{X} and \mathcal{Y} , which includes both classical and quantum correlations [49, 50]. From a quantum information point of view, the mutual information encodes the amount of information about the sub-system \mathcal{X} that can be obtained from the sub-system \mathcal{Y} . In this case, it is not necessary that $\mathcal{X} \cup \mathcal{Y} = \mathcal{E}$. For the specific results displayed in Sec. III B, i.e. the mutual information of the horizontal bonds we take $\mathcal{X} = \{(j, a)\}$, $\mathcal{Y} = \{(j+1, a)\}$ and for vertical bonds we take $\mathcal{X} = \{(j, a)\}$, $\mathcal{Y} = \{(j, \bar{a})\}$ in Eq. (B3) with $j = 1, a = 1$.

Appendix C: Effective Hamiltonian for $\Delta/\Omega \gg 1$

At $\Delta = \infty$, the spectrum of (1) is known exactly: all computational basis states (i.e. Fock states in the $\hat{\sigma}^z$ basis) are eigenstates of the Hamiltonian. To quantitatively study the effect of this integrable point near $\Delta \sim \Omega$, we construct a Schrieffer-Wolff (SW) rotation of the basis which shall make the effective Hamiltonian block diagonal in the eigenbasis of the diagonal part of the Hamilto-

nian $\hat{\mathcal{H}}_z$ up to first order in Ω/Δ . To this end we consider the generator of the SW rotation $i\hat{\mathcal{S}}$,

$$i\hat{\mathcal{S}} = -\frac{\Omega}{2i\Delta} \sum_{j=1}^L \sum_{a=1}^2 (-1)^j \hat{\sigma}_{j,a}^y \quad (\text{C1})$$

The structure of the generator $i\hat{\mathcal{S}}$ implies

$$[i\hat{\mathcal{S}}, \hat{\mathcal{H}}_z] = -\hat{\mathcal{H}}_x \quad (\text{C2})$$

The effective low-energy Hamiltonian, in the appropriate rotated basis reads

$$\hat{\mathcal{H}}_{\text{eff}}^{(2)} = -\frac{\Omega^2}{2\Delta} \sum_{j=1}^L \sum_{a=1}^2 (-1)^j \hat{\sigma}_{j,a}^z - \frac{\Omega^2}{4\Delta} \sum_{j=1}^L \sum_{a=1}^2 (-1)^j \hat{\mathcal{P}}_{j-1,a}^\downarrow \hat{\mathcal{P}}_{j-1,\bar{a}}^\downarrow \hat{\mathcal{P}}_{j+1,a}^\downarrow \hat{\mathcal{P}}_{j+1,\bar{a}}^\downarrow \hat{\mathcal{P}}_{j,a}^\downarrow \left(\hat{\sigma}_{j,a}^x \hat{\sigma}_{j,\bar{a}}^x + \hat{\sigma}_{j,a}^y \hat{\sigma}_{j,\bar{a}}^y \right) \quad (\text{C5})$$

Already at second order, the effective Hamiltonian provides us with a lot of intuition about the dominant physical processes taking place in the quench dynamics of the system. At this order, *any* allowed Fock state undergoes Rabi oscillations induced via the $XX + YY$ terms. This effective Hamiltonian also suggests the consideration of a number of “*emergent*” constants of motion for a system with $2L$ degrees of freedom. It is worth mentioning that, for a deeper understanding, it should be explored whether one can explicitly cast the effective Hamiltonian up to second order in a Bethe integrable form, and will be addressed in a future study. For example, consider Eq. (27) of the paper [51], which has a lot of similarity with the dynamical terms of the second order effective Hamiltonian. In their work, they cast the ansatz wavefunction in a coordinate Bethe ansatz form. Interestingly, this structure of the Hamiltonian also has close similarity with Eq. (2.10) of [52]. The models studied in [51, 52] both exhibit “*jamming*” and/or slow dynamics as a consequence of these additional conservation laws. The second-order effective Hamiltonian also gives rise to jamming and slow dynamics due to existence of the following extensive number of conservation laws (see Eq. (C7))

$$\begin{aligned} \hat{\mathcal{H}}_{\text{eff}} &= \hat{\mathcal{P}}_{Z_\pi} \left(e^{i\hat{\mathcal{S}}} \hat{\mathcal{H}} e^{-i\hat{\mathcal{S}}} \right) \hat{\mathcal{P}}_{Z_\pi} \\ &= \hat{\mathcal{H}}_{\text{eff}}^{(0)} + \hat{\mathcal{H}}_{\text{eff}}^{(1)} + \hat{\mathcal{H}}_{\text{eff}}^{(2)} + \hat{\mathcal{H}}_{\text{eff}}^{(3)} + \dots \end{aligned} \quad (\text{C3})$$

Where

$$\begin{aligned} \hat{\mathcal{H}}_{\text{eff}}^{(0)} &= \hat{\mathcal{P}}_{Z_\pi} \hat{\mathcal{H}}_z \hat{\mathcal{P}}_{Z_\pi}, \hat{\mathcal{H}}_{\text{eff}}^{(1)} = 0 \\ \hat{\mathcal{H}}_{\text{eff}}^{(2)} &= \hat{\mathcal{P}}_{Z_\pi} \left(\frac{1}{2!} [i\hat{\mathcal{S}}, \hat{\mathcal{H}}_x] \right) \hat{\mathcal{P}}_{Z_\pi} \\ \hat{\mathcal{H}}_{\text{eff}}^{(3)} &= \hat{\mathcal{P}}_{Z_\pi} \left(\frac{1}{3!} [i\hat{\mathcal{S}}, [i\hat{\mathcal{S}}, \hat{\mathcal{H}}_x]] \right) \hat{\mathcal{P}}_{Z_\pi} \\ \hat{\mathcal{H}}_{\text{eff}}^{(4)} &= \hat{\mathcal{P}}_{Z_\pi} \left(\frac{1}{4!} [i\hat{\mathcal{S}}, [i\hat{\mathcal{S}}, [i\hat{\mathcal{S}}, \hat{\mathcal{H}}_x]]] \right) \hat{\mathcal{P}}_{Z_\pi} \end{aligned} \quad (\text{C4})$$

In the above perturbation theory, all odd-order terms vanish and only even-order terms have a non-trivial contribution. By direct computation of the commutators, one arrives at the expression for $\hat{\mathcal{H}}_{\text{eff}}^{(2)}$

$$\hat{Z}_\pi = \sum_{j=1}^L \sum_{a=1}^2 (-1)^j \hat{\sigma}_{j,a}^z \quad (\text{C6})$$

$$\hat{Q}_j = \hat{\sigma}_{j,1}^z \hat{\sigma}_{j,2}^z \quad \forall j = 1, 2, \dots, L \quad (\text{C7})$$

Considering the conservation of the total energy, we have $L + 2$ number of constants of motion, which suggests that the effective Hamiltonian (up to second order) is integrable, and it is possible to write down explicitly the eigenvalues and eigenvectors of $\hat{\mathcal{H}}_{\text{eff}}^{[2]} = \hat{\mathcal{H}}_{\text{eff}}^{(0)} + \hat{\mathcal{H}}_{\text{eff}}^{(2)}$ in each charge sector labeled by the quantum numbers $\{z_\pi, q_1, q_2, \dots, q_L\}$. In the following section, we present an outline for the process of enumeration of all the eigenvectors and the eigenvalues of $\hat{\mathcal{H}}_{\text{eff}}^{[2]}$.

1. Full Spectrum of $\hat{\mathcal{H}}_{\text{eff}}^{[2]}$

First, we note by inspection that the vacuum state $|\text{vac}\rangle$ is annihilated by $\hat{\mathcal{H}}_{\text{eff}}^{[2]}$, the effective Hamiltonian up to second order i.e. $\hat{\mathcal{H}}_{\text{eff}}^{[2]} = \hat{\mathcal{H}}_{\text{eff}}^{(0)} + \hat{\mathcal{H}}_{\text{eff}}^{(2)}$. Now, we consider adding particles on top of the $|\text{vac}\rangle$ state by forming singlets/triplets of the following form

$$|j, \pm\rangle_{\text{IP}} = \frac{1}{\sqrt{2}} (|\dots \overset{\circ}{\bullet}_j \dots\rangle \pm |\dots \overset{\circ}{\bullet}_{\bar{j}} \dots\rangle) \quad (\text{C8})$$

where for brevity of notation, the dots “...” within the symbol $|\cdot\rangle$, imply absence of any Rydberg excitations/particles. The states $|j, \pm\rangle_{1P}, \forall j = 1, 2, \dots, L$ are *exact* eigenstates of $\hat{\mathcal{H}}_{\text{eff}}^{[2]}$ with eigenvalue $\pm 2\Delta - 3\Omega^2/4\Delta$. Similarly, one can construct two particle states on top of the $|\text{vac}\rangle$ state, with particles placed on neighboring sites (on alternate rungs) in the following way,

$$\begin{aligned} |j, 1\rangle_{2P} &= |\dots \circ \bullet_j \dots\rangle \\ |j, 2\rangle_{2P} &= |\dots \bullet_j \circ \dots\rangle \end{aligned} \quad (\text{C9})$$

which are zero modes of $\hat{\mathcal{H}}_{\text{eff}}^{[2]}, \forall j = 1, 2, \dots, L$. This construction can be generalized to many contiguous sites as follows,

$$\begin{aligned} |j, 1\rangle_{3P} &= |\dots \circ \bullet_j \circ \dots\rangle \\ |j, 2\rangle_{3P} &= |\dots \bullet_j \circ \bullet_j \dots\rangle \end{aligned} \quad (\text{C10})$$

Again the states, $|j, 1\rangle_{3P}$ and $|j, 2\rangle_{3P}, \forall j = 1, 2, \dots, L$ are eigenvectors of $\hat{\mathcal{H}}_{\text{eff}}^{[2]}$ and the energy eigenvalue has to be determined by inspection. This procedure can be continued to yield more eigenvectors of $\hat{\mathcal{H}}_{\text{eff}}^{[2]}$, until every other site in the ladder is filled, which leaves us with two eigenvectors $|\mathbb{Z}_2\rangle$ and $|\overline{\mathbb{Z}}_2\rangle$. Alternatively, one may also put non-contiguous excitations, which will again be exact eigenstates of the effective Hamiltonian

$$\begin{aligned} |(j_1, 1), (j_2, \pm)\rangle_{\text{nP}} &= \frac{1}{\sqrt{2}} (|\dots \circ \bullet_{j_1} \dots \bullet_{j_2} \dots\rangle \pm |\dots \bullet_{j_1} \circ \dots \bullet_{j_2} \dots\rangle) \\ |(j_1, 2), (j_2, \pm)\rangle_{\text{nP}} &= \frac{1}{\sqrt{2}} (|\dots \circ \bullet_{j_1} \dots \bullet_{j_2} \dots\rangle \pm |\dots \bullet_{j_1} \circ \bullet_{j_2} \dots\rangle) \end{aligned} \quad (\text{C11})$$

with the condition that the block of contiguous spins based to the left of site j_1 have at least one insertion of $|\circ\rangle$ between the excitations placed at site j_2 . Additionally, further non-zero modes of $\hat{\mathcal{H}}_{\text{eff}}^{[2]}$ can be constructed by placing “Bell-pair” like states which are separated by at least one insertion of $|\circ\rangle$ in between. Following these simple rules one may enumerate all eigenvectors of $\hat{\mathcal{H}}_{\text{eff}}^{[2]}$.

2. Storing classical bits of information

Utilizing the slow dynamics induced by the extensive number of approximate conservation laws, it is possible to store classical information, encoded via a class of appropriately chosen initial states which can be labeled uniquely in terms of the eigenvalues of “ L ”-quasi conserved charges in a square ladder with $N = 2L$ Rydberg atoms. This stored information can be retrieved at later times by performing simple projective readout measurements. To see how this can be achieved, consider a string of L -classical bits (c_1, c_2, \dots, c_L) where $c_i \in [-1, +1]$

$\forall i = 1, 2, \dots, L$, i being the rung index. Now, this classical string of information can be encoded as initial values of the approximately conserved local charges q_j 's at all rungs as $q_j = c_j$. As an example, in a ladder with $N = 2L = 12$ atoms, one can encode the classical information “bit-string” $(+1, +1, +1, -1, +1, -1, +1)$ in the initial quantum state $|\psi(0)\rangle = |\circ \bullet \circ \bullet\rangle$. This choice is not unique and the states $|\circ \bullet \circ \bullet\rangle, |\circ \bullet \circ \bullet\rangle, |\circ \bullet \circ \bullet\rangle$ are completely equivalent. In the course of full quantum dynamics via the Hamiltonian (1) for $\Delta \gg \Omega$, the expectation values of all \hat{Q}_j 's stay almost frozen, and more importantly do not change their sign, for times as large as $t\Omega \sim 10^4$, which is much beyond the time to which coherence can be maintained in experimental platforms. By a simple readout procedure, one can determine the sign of $\langle \hat{Q}_j \rangle_t$ at any time t during the experiment. By looking at this string of information, one can recover the encoded classical string (c_1, \dots, c_L) as

$$c_i = \frac{\langle \hat{Q}_i \rangle_t}{|\langle \hat{Q}_i \rangle_t|} \quad \forall i = 1, 2, \dots, L \quad (\text{C12})$$

From the structure of Eq. (C5), it is easy to interpret the form of the initial Fock state required to encode the bit-string (c_1, \dots, c_L) .

3. Ensemble of relaxation: Gibbs vs Generalized Gibbs

Under unitary quantum evolution via $\hat{\mathcal{H}}_{\text{eff}}^{[2]}$, the system preserves the following operators: $\hat{\mathcal{H}}_{\text{eff}}^{[2]}, \hat{\mathcal{Z}}_\pi$ and $\hat{Q}_j \forall j = 1, 2, \dots, L$. This implies, that if the system evolves purely via $\hat{\mathcal{H}}_{\text{eff}}^{[2]}$, at late times it should relax to the generalized Gibbs ensemble (GGE) described by appropriate Lagrange multipliers associated with these conservation laws (exact or approximate),

$$\hat{\rho}_{\text{GGE}} = \frac{1}{Z_{\text{GGE}}} \exp \left[-\beta \hat{\mathcal{H}}_{\text{eff}}^{[2]} - \lambda_\pi \hat{\mathcal{Z}}_\pi - \sum_{j=1}^L \lambda_j \hat{Q}_j \right] \quad (\text{C13})$$

where Z_{GGE} is a normalization factor which ensures that $\text{Tr}(\hat{\rho}_{\text{GGE}}) = 1$. On the other hand, as the additional extensive number of conservation laws are only approximate, the system (which evolves via the Hamiltonian (1)) should relax (at very late times set by the fourth order effective Hamiltonian) to the Gibbs ensemble

$$\hat{\rho}_{\text{GE}} = \frac{1}{Z_{\text{GE}}} \exp \left[-\beta \hat{\mathcal{H}} \right] \quad (\text{C14})$$

where Z_{GE} is a normalization constant such that $\text{Tr}(\hat{\rho}_{\text{GE}}) = 1$. For both cases, the relevant Lagrange multipliers i.e. $\{\beta, \lambda_\pi, \lambda_{1,2,\dots,L}\}$ for GGE and β for GE, are determined by requiring the equality of the initial

values of the conserved charges to the expectation values of conserved operators with respect to this ensemble. In practice, we have done this by minimizing the related cost functions $f_{\text{GGE}}(\{\beta, \lambda_\pi, \lambda_{1,2,\dots,L}\})$ and $f_{\text{GE}}(\beta)$ using numerical solvers [53]

$$f_{\text{GE}}(\beta) = \left(\text{Tr} \left(\hat{\rho}_{\text{GGE}} \hat{\mathcal{H}} \right) - \text{Tr} \left(\hat{\rho}_0 \hat{\mathcal{H}} \right) \right)^2 \quad (\text{C15})$$

$$f_{\text{GGE}}(\{\beta, \lambda_\pi, \vec{\lambda}\}) = \sum_{\eta} \left(\text{Tr} \left(\hat{\rho}_{\text{GGE}} \hat{\mathcal{I}}_{\eta} \right) - \text{Tr} \left(\hat{\rho}_0 \hat{\mathcal{I}}_{\eta} \right) \right)^2 \quad (\text{C16})$$

Where $\{\hat{\mathcal{I}}_{\eta}\}$ collectively stands for all the conserved quantities of $\hat{\mathcal{H}}_{\text{eff}}^{[2]}$, $\hat{\rho}_0$ is the initial density operator and the dependence of $\hat{\rho}_{\text{GGE}/\text{GGE}}$ on the Lagrange multipliers is implicitly assumed.

Appendix D: 3-leg ladder

We now focus on a new model which is related to the 2-leg square ladder in a simple way. We now consider the 3-leg ladder with the same staggered detuning pattern along the longer direction of the lattice and study the nature of quantum quench dynamics for a range of parameter values. As before we consider periodic boundary conditions, and the Hamiltonian now reads

$$\hat{\mathcal{H}}_{3\text{-leg}} = \Omega \sum_{j=1}^L \sum_{a=1}^3 \hat{\sigma}_{j,a}^x - \Delta \sum_{j=1}^L \sum_{a=1}^3 (-1)^j \sigma_{j,a}^z \quad (\text{D1})$$

where $\hat{\sigma}_{j,a}^{\alpha} \equiv \hat{\mathcal{P}}_{j+1,a}^{\downarrow} \hat{\mathcal{P}}_{j-1,a}^{\downarrow} \hat{\mathcal{P}}_{j,a-1}^{\downarrow} \hat{\mathcal{P}}_{j,a+1}^{\downarrow} \hat{\sigma}_{j,a}^{\alpha}$ with $\alpha = (x, y, z)$

1. Quantum many-body scars

We now consider quantum quench dynamics starting from simple initial product state (in Fock/computational

basis). Due to the periodic boundary condition, it is not possible to accommodate the Néel state $|\mathbb{Z}_2\rangle$ on a lattice with odd number of legs without violating the Rydberg blockading constraint. For this reason we do not consider the quantum quench dynamics at $\Delta = 0$ in this case since for the 2-leg ladder it was the Néel state which showed anomalous revivals for this parameter choice. We shall instead focus on the dynamics from other initial states which are allowed in a 3-leg ladder configuration of the lattice such as $|\text{vac}\rangle \equiv \left| \begin{smallmatrix} \circ\circ\circ\circ\circ \\ \circ\circ\circ\circ\circ \\ \circ\circ\circ\circ\circ \end{smallmatrix} \right\rangle$ and the $|1\text{P}\rangle \equiv \left| \begin{smallmatrix} \circ\circ\circ\circ\circ \\ \circ\circ\bullet\circ\circ \\ \circ\circ\circ\circ\circ \end{smallmatrix} \right\rangle$ state at $\Delta = 1$.

As Fig. 20 top pane illustrates, for the case of the 3-leg ladder $|\text{vac}\rangle$ shows anomalous revivals which the other state do not. Here for the $|\text{vac}\rangle$ state one has $\langle \text{vac} | \hat{\mathcal{H}}_{3\text{-leg}} | \text{vac} \rangle = 0$ which, combined with the fact that the spectrum of (D1) has a spectral reflection symmetry implies that the system should relax to an infinite temperature ($\beta_{\text{vac}} = 0$) Gibbs ensemble. In contrast, for the $|1\text{P}\rangle$ state, the initial energy density is $\langle 1\text{P} | \hat{\mathcal{H}}_{3\text{-leg}} | 1\text{P} \rangle = -2\Delta$, which corresponds to a Gibbs ensemble of inverse temperature $\beta_{1\text{P}} \simeq -10^{-5}$, however this state does not show any anomalous persistent revivals in the return probability.

2. Emergent Conservation Laws and Slow Dynamics $\Delta/\Omega \gg 1$

For $\Delta/\Omega \gg 1$ the low-energy effective Hamiltonian can be obtained by in the same way as in Appendix-C by considering a 3-leg version of the generator for SW rotations (see Eq. (C1)). As before, the rotation ensures there are no high-energy processes in first-order and the term corresponding to the second-order effective Hamiltonian now has the form (D2). Similar to the 2-leg case, the effective low-energy Hamiltonian in this case (D2) only allows a specific spin-flip processes to take place if a ‘‘blockading’’ condition is satisfied. This specific blockading constraint and the spin-flip process can be understood in the same way as for the 2-leg case by considering the terms involving $\hat{\sigma}^{x/y}$ in the second-order effective Hamiltonian which is given below (see Eq. D2). We have assumed periodic boundary conditions in both directions which implies $a - 2 \equiv a + 1$ and $a + 2 \equiv a - 1$ for $a = 1, 2, 3$ in a 3-leg ladder.

$$\begin{aligned} \hat{\mathcal{H}}_{3\text{-leg,eff}}^{[2]} = & -\frac{\Omega^2}{2\Delta} \sum_{j,a} (-1)^j \hat{\sigma}_{j,a}^z - \frac{\Omega^2}{4\Delta} \sum_{j,a} \sum_{j',a'} (-1)^j \left[\hat{\mathcal{P}}_{j-1,a-1}^{\downarrow} \hat{\mathcal{P}}_{j+1,a-1}^{\downarrow} \hat{\mathcal{P}}_{j,a-2}^{\downarrow} \hat{\mathcal{P}}_{j-1,a}^{\downarrow} \hat{\mathcal{P}}_{j,a+1}^{\downarrow} \hat{\mathcal{P}}_{j,a}^{\downarrow} \hat{\mathcal{P}}_{j,a}^{\downarrow} (\hat{\sigma}_{j,a}^y \hat{\sigma}_{j,a-1}^y + \hat{\sigma}_{j,a}^x \hat{\sigma}_{j,a-1}^x) \right] \\ & + (-1)^j \left[\hat{\mathcal{P}}_{j-1,a+1}^{\downarrow} \hat{\mathcal{P}}_{j+1,a+1}^{\downarrow} \hat{\mathcal{P}}_{j-1,a}^{\downarrow} \hat{\mathcal{P}}_{j+1,a}^{\downarrow} \hat{\mathcal{P}}_{j,a-1}^{\downarrow} \hat{\mathcal{P}}_{j,a+2}^{\downarrow} \hat{\mathcal{P}}_{j,a}^{\downarrow} (\hat{\sigma}_{j,a}^y \hat{\sigma}_{j,a+1}^y + \hat{\sigma}_{j,a}^x \hat{\sigma}_{j,a+1}^x) \right] \end{aligned} \quad (\text{D2})$$

As a consequence, a class of initial states (specific Fock

states) exhibit a simple motion that can be described by

only considering the “blockaded-hopping” of the Rydberg excitations on the sites of the lattice allowed by $\hat{\mathcal{H}}_{3\text{-leg,eff}}^{[2]}$ for times before the effects of the fourth-order terms of the perturbative Hamiltonian sets in (see bottom panel of Fig. 20). For the initial state $|1P\rangle \equiv \left| \begin{array}{c} \bullet \circ \circ \circ \circ \\ \circ \circ \circ \circ \circ \\ \circ \circ \circ \circ \circ \end{array} \right\rangle$, evolving under the action of $\hat{\mathcal{H}}_{3\text{-leg,eff}}^{[2]}$, at any instant of time t , the quantum state can be written in the form $|\psi(t)\rangle = \ell_1(t)|1,1\rangle + \ell_2(t)|1,3\rangle + \ell_3(t)|1,3\rangle$, with $|\ell_3(t)| = |\ell_2(t)|$ where $|(j,a)\rangle$ denotes the one particle state with the particle/Rydberg excitation on the site (j,a) of the 3-leg ladder which can be clearly seen from the bottom panel of Fig. 20.

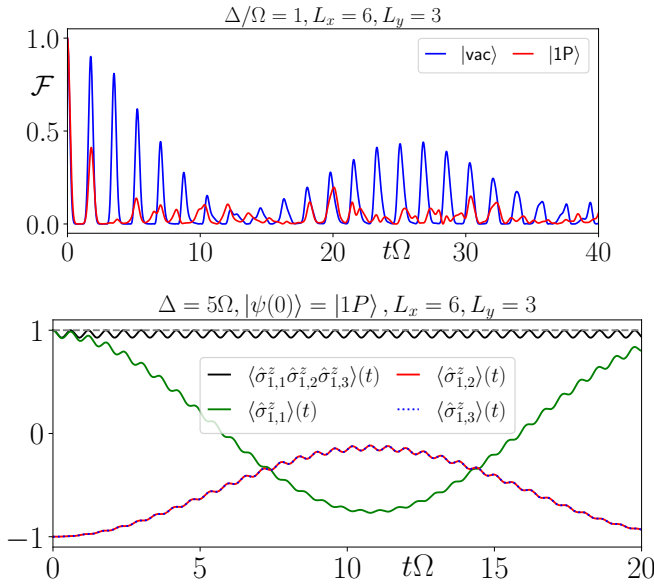


FIG. 20. (Top panel) Return probability $\mathcal{F}(t) = |\langle \psi(0) | \psi(t) \rangle|^2$ starting from different initial states for $\Delta/\Omega = 1$ on a 3-leg ladder (see Eq. (D1)) with periodic boundary conditions. (Bottom panel) Illustration of 3-body conservation law $\langle \hat{\sigma}_{1,1}^z \hat{\sigma}_{1,2}^z \hat{\sigma}_{1,3}^z \rangle(t)$ (black solid curve) for the 3-leg ladder starting from a different one particle state i.e. $|1P\rangle \equiv \left| \begin{array}{c} \bullet \circ \circ \circ \circ \\ \circ \circ \circ \circ \circ \\ \circ \circ \circ \circ \circ \end{array} \right\rangle$. In this case, the product of $\hat{\sigma}^z$'s on each rung behaves as an emergent conserved quantity. The state has been evolved using a discrete time-step integrator [29].

As a consequence of such an evolution the 3-body operator $\hat{\sigma}_{1,1}^z \hat{\sigma}_{1,2}^z \hat{\sigma}_{1,3}^z$ remains approximately conserved throughout the quantum evolution at $\Delta/\Omega = 5$. This is qualitatively similar to the 2-leg square ladder case, where product of 2-body spin operators remained approximately conserved. Thus, the results described in the main text for a 2-leg square ladder can be easily extended for a 3-leg square ladder with staggered detuning along the horizontal direction.

Appendix E: van der Waals interactions and validity of the first nearest neighbor Rydberg Blockade

In a Rydberg atom quantum simulator setup (such as in [2, 7]), neutral alkali atoms are trapped and arranged in a desired lattice geometry (such as in Fig. 1) with optical tweezer arrays, and are driven off-resonantly (with site-dependent detunings $\Delta_{\vec{r}}$) with a laser gives rise effective Rabi oscillations between the ground $|G\rangle$ and the Rydberg excited state $|R\rangle$ with frequency 2Ω . The Hamiltonian of the system reads

$$\hat{\mathcal{H}}_{\text{Ryd}}^{\text{Full}} = \sum_{\vec{r}} (\Omega \hat{\sigma}_{\vec{r}}^x - \Delta_{\vec{r}} \hat{\sigma}_{\vec{r}}^z) + \frac{V_0}{2} \sum_{\vec{r}, \vec{r}'} \frac{\hat{n}_{\vec{r}} \hat{n}_{\vec{r}'}}{|\vec{r} - \vec{r}'|^6} \quad (\text{E1})$$

where \vec{r} denotes the position vectors of the trapped atoms, which can be thought of as sites of a lattice. Furthermore, we have assumed that the electronic excited states for the atom is $|R\rangle = |nS\rangle$. When the atoms are in their Rydberg excited states, they experience an isotropic long-range repulsive van der Waals interaction (vdW) which falls off as $1/d^6$ where d is the separation between the excited atoms. The last double sum is taken over all possible pairs of atoms placed on sites \vec{r}, \vec{r}' of the ladder with $N = 2L$ sites and $\hat{n}_{\vec{r}} = (\hat{\sigma}_{\vec{r}}^z + 1)/2 = |R\rangle_{\vec{r}} \langle R|$ is the projection operator corresponding to the Rydberg excited state $|R\rangle$ at site \vec{r} .

In order to have an understanding of how accurately the idealized kinetically constrained models mimic the features of the fully interacting long-range system, we present a direct comparison between them. First, we briefly revisit the 1D Rydberg chain and the associated 1D PXP model (Appendix-E1), and then come to the case of the 2-leg square ladder (Appendix-E2) and then we briefly discuss the existence of Rydberg blockaded regime when the Rydberg atoms are arranged in a 2D square lattice with a staggered detuning along the longer direction (Appendix-E3).

1. 1D Rydberg Chain

The Rydberg blockading regime can be realized from (E1), if the repulsive vdW interaction energy is much higher than other energy scales of the system. In such a scenario the system can be described by a simpler effective Hamiltonian obtained by perturbative arguments [23]. In order to understand how accurately, the effective Hamiltonian in a constrained Hilbert space represents the dynamics of the full system as depicted by Eq. (E1), we first focus on the paradigmatic PXP chain with site-dependent detunings Δ_j (henceforth referred to as the PXP+Z model) and the related fully interacting long-range model. The fully interacting long-range Hamiltonian for the 1D chain is the one dimensional analogue of Eq. (E1), whereas in the limit $V_0 \gg \Delta_j, \Omega$ the low-energy effective Hamiltonian reads

$$\hat{\mathcal{H}}_{\text{Ryd}}^{\text{eff}} = \sum_{j=1}^L \left(\Omega \hat{\sigma}_j^x - \Delta_j \hat{\sigma}_j^z \right) + \frac{V_0}{2} \sum_{j,j' > \text{NN}_1} \frac{\hat{n}_j \hat{n}_{j'}}{|j-j'|^6} \quad (\text{E2})$$

Here the double sum in the equation above is over all pairs of sites which are not nearest neighbors of each other. If the parameters V_0, Ω, Δ_j are such that $V_0 \gg \Delta_j, \Omega \gg V_0/2^6$, then the repulsive interaction term in (E2) is extremely small and the evolution of the system is entirely captured by the PXP+Z model. Such a situation is achieved by taking $\Delta_j, \Omega \sim 1$ and $V_0 = 10\Omega$, in which case the condition $V_0 \gg \Delta_j, \Omega \gg V_0/2^6$ is satisfied in an order of magnitude sense. If, however, $V_0/2^6$ is not negligible compared to Δ_j, Ω , then the repulsive interaction term is going to play a significant role in the approximate evolution of the full system and needs to be considered. This is the case if, for example, the parameters are such that $V_0 \gg \Delta_j, \Omega \gg V_0/3^6$ and we can only neglect long-range interactions at distances greater than two lattice separation units, in which case the Hamiltonian (E2) further simplifies to a short-range interacting Hamiltonian with the following form

$$\hat{\mathcal{H}}_{\text{Ryd}}^{\text{eff}, \text{NN}_2} = \sum_{j=1}^L \left(\Omega \hat{\sigma}_j^x - \Delta_j \hat{\sigma}_j^z \right) + \frac{V_0}{2} \sum_{j,j' \in \text{NN}_2} \frac{\hat{n}_j \hat{n}_{j'}}{|j-j'|^6} \quad (\text{E3})$$

Here $j, j' \in \text{NN}_2$ means that the double sum only contains the j, j' pairs which are separated by exactly two lattice separation units.

In Fig. 21 we show a comparison of the Hamiltonians (E1), (E3): the left panel shows that the low-energy part of the spectrum of the full long-range interacting system (E1) can be faithfully captured by the entire spectrum of the kinetically constrained Hamiltonian (PXP+Z model). As the inset of this panel demonstrates, there is no qualitative difference in the energy eigenvalues even when the second nearest neighbor interactions (Eq. (E3)) are considered beyond the Rydberg blockade regime. The right panel Fig. 21 shows the quantum evolution of the system starting from the Néel state and we can conclude that, although the qualitative features remain the same, there are quantitative differences in the behaviors predicted by (E1), (E3) and the kinetically constrained model with no additional vdW interactions (which is the PXP+Z model in this case). Comparison of both spectral as well as dynamical features of these three descriptions indicate that the PXP+Z model provides a good qualitative description of the full long-range interacting many-body system described by Eq (E1).

2. 2-leg Rydberg Square Ladder

We now investigate the validity of the specific Rydberg blockade constraint for the 2-leg square ladder system,

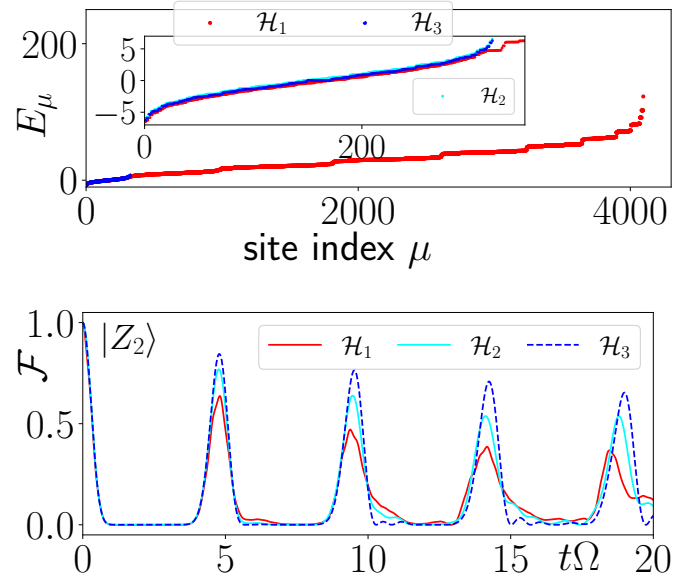


FIG. 21. 1D Rydberg chain as captured via the Hamiltonians (E1), (E3) and the PXP+Z model (denoted in the legend by $\hat{\mathcal{H}}_1, \hat{\mathcal{H}}_2$ and $\hat{\mathcal{H}}_3$ respectively) for $N = 12$ atoms and $V_0 = 10\Omega$: (top panel) spectrum and (bottom panel) evolution of the return probability starting from the Néel state. See text for details.

that was assumed throughout the main text (see Fig. 1), by considering the full long-range interacting system and its various approximations. The fully interacting long-range system is now given by the 2-leg square ladder version of Eq. (E1) while the low-energy effective Hamiltonian in the limit $V_0 \gg \Delta_{j,a}, \Omega$ now reads

$$\hat{\mathcal{H}}_{\text{Ryd}}^{\text{eff}} = \sum_{j=1}^L \sum_{a=1}^2 \left(\Omega \hat{\sigma}_{j,a}^x - \Delta_{j,a} \hat{\sigma}_{j,a}^z \right) + \frac{V_0}{2} \sum_{\vec{r}, \vec{r}' > \text{NN}_1} \frac{\hat{n}_{\vec{r}} \hat{n}_{\vec{r}'}}{|\vec{r} - \vec{r}'|^6} \quad (\text{E4})$$

It is crucial here to note that the second nearest neighbor distance between two atoms in this case is $\sqrt{2}$ (in lattice separation units). This implies that for the 2-leg square ladder geometry, the conditions which the parameters $V_0, \Delta_{j,a}, \Omega$ must satisfy so that the long-range interactions beyond the first neighbor could be neglected is $V_0 \gg \Delta_{j,a}, \Omega \gg V_0/(\sqrt{2})^6$. However, this condition cannot be met even in an order of magnitude sense, as can be seen, for example, by taking $\Omega, \Delta_{j,a} \sim 1, V_0 = 10\Omega$ which is required to satisfy $V_0 \gg \Delta_{j,a}, \Omega$, but makes it impossible to satisfy $\Delta_{j,a}, \Omega \gg V_0/(\sqrt{2})^6$. This leads us to believe that, the specific form of the constraint assumed throughout the main text, could be in practice difficult to achieve in actual experiments in a Rydberg atom quantum simulator platform.

To illustrate this, in Fig. 22 we compare the evolution of fidelity starting from the Néel state, under the fully

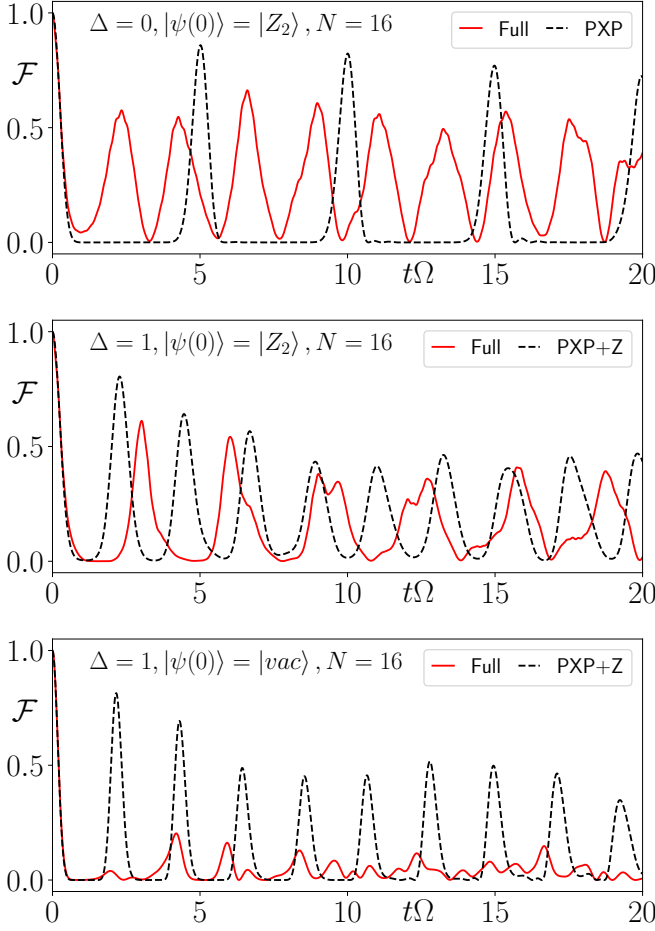


FIG. 22. Comparison of the return probability $\mathcal{F} = |\langle \psi(0) | \psi(t) \rangle|^2$ by evolving an initial state under the fully interacting long-range Hamiltonian (E1) (red solid line) taking $V_0 = 10\Omega$ and the idealized kinetically constrained system 2D PXP+Z model (1) (black dashed lines) for $N = 16$ atoms. The specific initial conditions are as follows: (top panel) $|\psi(0)\rangle = |Z_2\rangle$, $\Delta = 0$ (middle panel) $|\psi(0)\rangle = |Z_2\rangle$, $\Delta/\Omega = 1$ and (bottom panel) $|\psi(0)\rangle = |\text{vac}\rangle$, $\Delta/\Omega = 1$. In all cases the states have been evolved via exact diagonalization method.

interacting long-range Hamiltonian (E1), and the kinetically constrained Hamiltonian (1). This figure shows that even the qualitative nature of quantum dynamics of these two Hamiltonians (E1) and (1) are quite different each other, and hence we come to the conclusion that, the kinetic constraint illustrated in Fig. 1, is not a faithful representation of the actual long-range interacting system that would be realized in an experimental setup.

$$\hat{\mathcal{H}}_{\text{Ryd}}^{\text{eff, NN}_2} = \sum_{j=1}^L \sum_{a=1}^2 \left(\Omega \hat{\sigma}_{j,a}^x - \Delta_{j,a} \hat{\sigma}_{j,a}^z \right) + \frac{V_0}{2} \sum_{\vec{r}, \vec{r}' \in \text{NN}_2} \frac{\hat{n}_{\vec{r}} \hat{n}_{\vec{r}'}}{|\vec{r} - \vec{r}'|^6} \quad (\text{E5})$$

From Fig. 22 bottom panel it is clear that the $|\text{vac}\rangle$ state does not show any anomalous revivals when the full long-range interacting system is considered. However,

as Figs. 22 top and middle panel demonstrate, the $|Z_2\rangle$ state shows a substantial degree of anomalous oscillation lasting several cycles, which cannot be explained from the PXP+Z approximation.

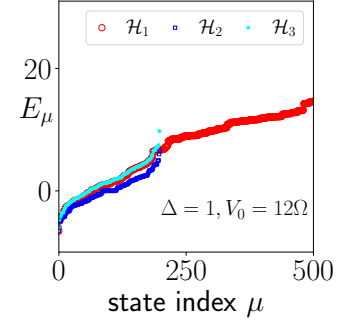


FIG. 23. Comparison of the eigenvalues of the three Hamiltonians (E1), (E5) and (E6) (denoted by $\hat{\mathcal{H}}_1$, $\hat{\mathcal{H}}_2$ and $\hat{\mathcal{H}}_3$ in the legend respectively) for $\Delta = 1$, $V_0 = 12\Omega$. Only the low-energy part of the spectrum has been displayed.

However, these oscillations can be qualitatively described by augmenting the PXP+Z model with second nearest neighbor vdW interactions as in (E5). This conclusion is further supported by the fact that considering a short-range interacting system governed by the Hamiltonian (E5), which is obtained from (E4) by considering interactions only up to the second-nearest neighbors, seems to capture both the spectral and dynamical features of the fully interacting long-range Hamiltonian (E1) (see Fig. 23, Fig. 24)

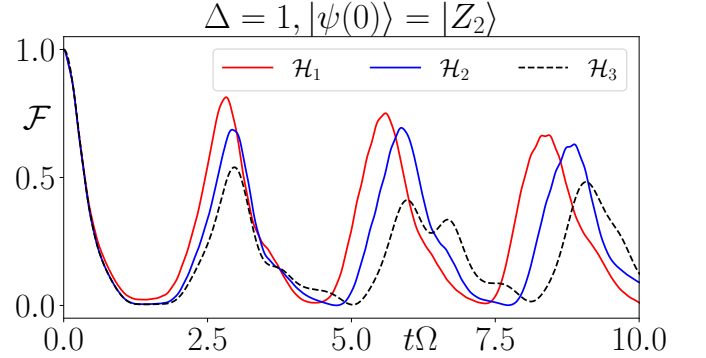


FIG. 24. Comparison of the return probability $\mathcal{F} = |\langle \psi(0) | \psi(t) \rangle|^2$ computed by evolving the initial state $|\psi(0)\rangle = |Z_2\rangle$ state via three different Hamiltonians (E1), (E5), (E6) (denoted by $\mathcal{H}_1, \mathcal{H}_3, \mathcal{H}_2$ in the legend respectively) for a system of $N = 12$ atoms with $\Delta = 1$, $V_0 = 12\Omega$ (see text for details) In all cases the state has been evolved by a discrete time-step integration method [29].

In Fig. 24 the return probability $\mathcal{F} = |\langle \psi(0) | \psi(t) \rangle|^2$ starting from the $|Z_2\rangle$ state is shown as a function of time by evolving the state under the Hamiltonian (E1) (red solid line), (E5) (black dashed line) and (E6) (blue solid

line) for a system with $N = 12$ atoms at $\Delta = 1$. Thus for reasons mentioned above the second nearest-neighbor vdW interactions are essential in understanding the qualitative features of quantum dynamics depicted by the full long-range interacting system.

$$\hat{\mathcal{H}}_{\text{Ryd}}^{\text{eff,NN}_2} = \sum_{j=1}^L \sum_{a=1}^2 (\Omega \hat{\sigma}_{j,a}^x - \Delta_{j,a} \hat{\sigma}_{j,a}^z) + \frac{V_0}{2} \sum_{\vec{r}, \vec{r}' \in \text{NN}_{1,2}} \frac{\hat{n}_{\vec{r}} \hat{n}_{\vec{r}'}}{|\vec{r} - \vec{r}'|^6} \quad (\text{E6})$$

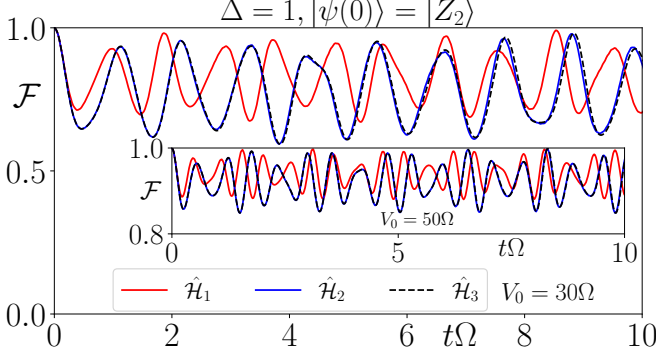


FIG. 25. Comparison of the return probability $\mathcal{F} = |\langle \psi(0) | \psi(t) \rangle|^2$ computed by evolving the initial state $|\psi(0)\rangle = |Z_2\rangle$ state via three different Hamiltonians (E1), (E5), (E6) (denoted by $\mathcal{H}_1, \mathcal{H}_3, \mathcal{H}_2$ in the legend respectively) for a system of $N = 12$ atoms with $\Delta = 1, V_0 = 30\Omega$ (main) and $\Delta = 1, V_0 = 50\Omega$ (inset) respectively (see text for details) In all cases the state has been evolved by a discrete time-step integration scheme [29]

It is also worth noting that increasing the strength of the vdW repulsive interaction (or equivalently reducing the lattice constant), increases the configurational energy of the Néel state (i.e., $\langle Z_2 | \hat{\mathcal{H}}_{\text{Ryd}}^{\text{Full}} | Z_2 \rangle$) and results in confinement of this state (see Fig. 25). From the comparison between the dynamics obtained from the three different Hamiltonians (E1), (E6), (E5), we can conclude that the confinement is a consequence of next nearest neighbor interaction, since the dynamics of the Néel state obtained by evolving the state via Hamiltonians (E5), (E6) agree qualitatively with that obtained from the fully interacting long-range system governed by (E1).

3. Two Dimensional Square Lattice

The two dimensional (2D) PXP model has been shown to host QMBS [54]. However, the inability of the kinetically constrained model such as (1), to faithfully represent the quantum dynamics of the fully interacting long-range system (E1) for a 2-leg ladder geometry (see Appendix-E), brings into question the existence of QMBS in a physical two-dimensional Rydberg atom simulator in

which vdW interactions are always present. The Hamiltonian for the 2D PXP+Z model (with site dependent detunings $\Delta_{j,a} = (-1)^j \Delta$) of dimension $L_x \times L_y$ is given by

$$\hat{\mathcal{H}}_{\text{PXP+Z}}^{2\text{D}} = \Omega \sum_{j=1}^{L_x} \sum_{a=1}^{L_y} \hat{\sigma}_{j,a}^x - \Delta \sum_{j=1}^{L_x} \sum_{a=1}^{L_y} (-1)^j \hat{\sigma}_{j,a}^z \quad (\text{E7})$$

where $\hat{\sigma}_{j,a}^x \equiv \hat{\mathcal{P}}_{j+1,a}^\dagger \hat{\mathcal{P}}_{j-1,a}^\dagger \hat{\mathcal{P}}_{j,a-1}^\dagger \hat{\mathcal{P}}_{j,a+1}^\dagger \hat{\sigma}_{j,a}^x$

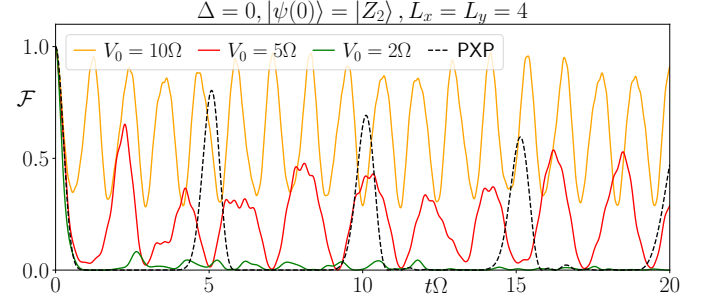


FIG. 26. Comparison of the return probability $\mathcal{F} = |\langle \psi(0) | \psi(t) \rangle|^2$ as function of time t starting from the Néel state in the 2D geometry for a 4×4 square lattice, computed with (i) full long-range interacting system (solid curves) with different vdW interaction strengths $V_0 = 10\Omega$ (orange), $V_0 = 5\Omega$ (red), $V_0 = 2\Omega$ (green) and (ii) the idealized 2D PXP approximation (black dashed line) for $\Delta = 0$ (see text for details). In all cases the states have been evolved via a discrete time-step integration scheme

Fig. 26 shows the comparison of the return probability of the initial Néel state ($|Z_2\rangle$) when evolved via the Hamiltonian Eq. (E7) (dashed black curve) with the corresponding results of the long-range interacting system for $V_0 = 10\Omega$ (orange curve), $V_0 = 5\Omega$ (red curve). The parameter choices $V_0 = 10\Omega$ or $V_0 = 5\Omega$ satisfies the condition $V_0 \gg \Omega$ in a qualitative sense, however, the kinetically constrained model Hamiltonian does not capture the same dynamical behavior.

We now turn on a non-zero staggered detuning ($\Delta \neq 0$) and ask if the anomalous revivals from the $|Z_2\rangle$ and $|\text{vac}\rangle$ state observed for the 2-leg square ladder geometry [24], has any analogue in the 2D square lattice scenario.

From Fig. 27 we can see that in 2D the PXP+Z approximation given by Eq. (E7) does not fully capture the features of the full long-range interacting system accurately for $V_0 = 2\Omega, 5\Omega$ and 10Ω . The disagreement is more severe for the Rydberg vacuum initial state, as the PXP+Z predicts persistent oscillations lasting several cycles while the full long-range interacting system predicts this state does not have any noticeable revivals. This again leads us to conclude that for geometries in which the second nearest-neighbor distance is $\sqrt{2}$ (in

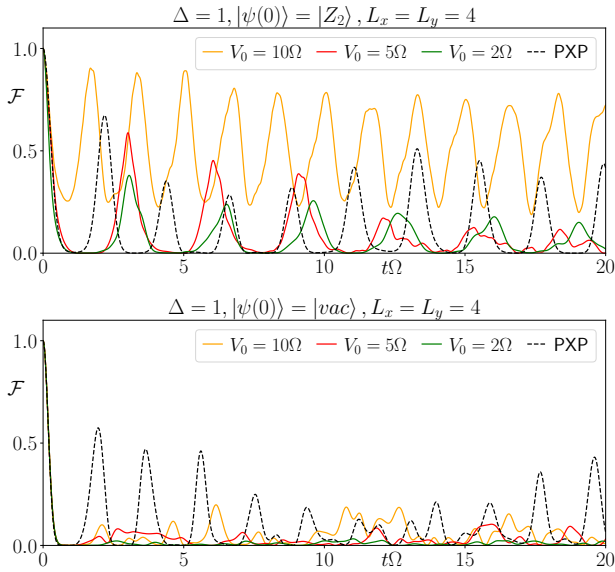


FIG. 27. Comparison of the return probability $\mathcal{F} = |\langle \psi(0) | \psi(t) \rangle|^2$ as function of time t starting from (top panel) the Néel state $|Z_2\rangle$ and (bottom panel) the Rydberg vacuum state $|vac\rangle$ in the 2D geometry for a 4×4 square lattice, computed with (i) full long-range interacting system (solid curves) with different vdW interaction strengths $V_0 = 10\Omega$ (orange), $V_0 = 5\Omega$ (red), $V_0 = 2\Omega$ (green) and (ii) the idealized 2D PXP approximation given by Eq. (E7) (black dashed line) for $\Delta/\Omega = 1$ (see text for details). In all cases the states have been evolved via a discrete time-step integration scheme.

lattice separation units), the idealized strong Rydberg blockaded models do not faithfully capture the dynamics in these systems.

We end this section by noting that, realizing such geometric blockades, could in principle be made easier to achieve by leveraging anisotropic interactions as shown to exist for more complex Rydberg excited electronic states [42]. However, such systems exhibit completely different kinds of effective spin interactions and the associated dynamics will exhibit vastly different phenomena.

Appendix F: Scaling of the norm of rescaled, regularized Adiabatic Gauge Potential (AGP)

The adiabatic gauge potential (AGP) is defined as the generator of adiabatic evolution of the eigenstates of the Hamiltonian, when some parameters of the Hamiltonian are varied. As in the rest of this paper, we are concerned with the behavior of the model (1), when $\Omega = 1$, and Δ is varied, here we shall focus on the AGP $\hat{\mathcal{A}}_\Delta$ defined as

$$\hat{\mathcal{A}}_\Delta |E_\mu(\Delta)\rangle = i\partial_\Delta |E_\mu(\Delta)\rangle \quad (\text{F1})$$

Where $\hat{\mathcal{H}}(\Delta) |E_\mu(\Delta)\rangle = E_\mu(\Delta) |E_\mu(\Delta)\rangle$ to understand whether the model given by Eq. (1) is chaotic for finite

values of Δ at times which are exponentially large in system size. The regularized AGP norm then reads [30]

$$\|\hat{\mathcal{A}}_\Delta\|^2 = \frac{1}{D_H} \sum_\nu \sum_{\mu \neq \nu} \frac{\omega_{\mu\nu}^2}{(\omega_{\mu\nu}^2 + \zeta^2)^2} |\langle E_\mu | \partial_\Delta \hat{\mathcal{H}} | E_\nu \rangle|^2 \quad (\text{F2})$$

In the above equation, the sum on μ, ν runs over the Hilbert space (which may or may not be symmetry-reduced) and $\zeta \propto N \log(N)$ is a cutoff introduced to regularize singularities arising due to degeneracies in the spectrum and $\omega_{\mu\nu} \equiv E_\mu - E_\nu$. The advantage of introducing this ultraviolet regulator ζ , ensures that even if the symmetries of the Hamiltonian are not completely resolved, the regularized AGP norm gives a meaningful answer. In contrast almost all alternative measures of spectral statistics which are readily used as probes of the onset of quantum chaos (see Ref. [55]) where the knowledge and resolution of all symmetries of the Hamiltonian is essential. We note that the spectral form factor is an important exception, but necessarily relies on the introduction of disorder in the system to extract a clean signature for the onset of quantum chaos (the dip-ramp-plateau structure [56]).

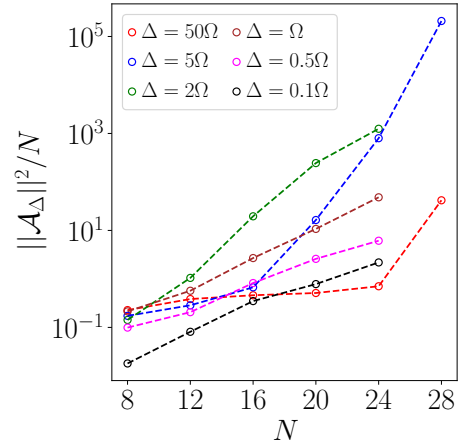


FIG. 28. Behavior of the rescaled, regularized AGP norm for a range of values of Δ/Ω for system sizes $N = 8, 12, 16, 20, 24, 28$. In all cases $\|\hat{\mathcal{A}}_\Delta\|^2/N$ increases in an exponential fashion as larger system sizes are accessed, which indicates that the Hamiltonian (1) is as a whole, quantum chaotic, even if ergodicity breaking features of various forms exist for specific states and finite-size systems.

In Fig. 28 we show the rescaled norm of the regularized AGP i.e. $\|\hat{\mathcal{A}}_\Delta\|^2/N$, for a range of system sizes $N = 8 - 28$. This figure illustrates that $\|\hat{\mathcal{A}}_\Delta\|^2/N$ grows with N in an exponential fashion for all regimes of Δ . This exponential growth becomes noticeable only for larger system sizes when we are in the regime of emergent approximate conservation laws ($\Delta \gg \Omega$) as seen by the data for $\Delta = 5\Omega$ (blue open circles) and $\Delta = 50\Omega$

(red open circles). In contrast for lower values of Δ/Ω such as $\Delta = 2\Omega$ (green open circles), $\Delta = \Omega$ (brown open circles), $\Delta = 0.5\Omega$ (magenta open circles) and $\Delta = 0.1\Omega$

(black open circles) the exponential growth seems noticeable even for small system sizes.

-
- [1] H. Weimer, M. Müller, I. Lesanovsky, P. Zoller, and H. P. Büchler, A rydberg quantum simulator, *Nature Physics* **6**, 382 (2010).
- [2] H. Bernien, S. Schwartz, A. Keesling, H. Levine, A. Omran, H. Pichler, S. Choi, A. S. Zibrov, M. Endres, M. Greiner, V. Vuletić, and M. D. Lukin, Probing many-body dynamics on a 51-atom quantum simulator, *Nature* **551**, 579 (2017).
- [3] T. L. Nguyen, J. M. Raimond, C. Sayrin, R. Cortiñas, T. Cantat-Moltrecht, F. Assemat, I. Dotsenko, S. Gleyzes, S. Haroche, G. Roux, T. Jolicoeur, and M. Brune, Towards quantum simulation with circular rydberg atoms, *Phys. Rev. X* **8**, 011032 (2018).
- [4] A. Browaeys and T. Lahaye, Many-body physics with individually controlled rydberg atoms, *Nature Physics* **16**, 132 (2020).
- [5] P. Scholl, M. Schuler, H. J. Williams, A. A. Eberharter, D. Barredo, K.-N. Schymik, V. Lienhard, L.-P. Henry, T. C. Lang, T. Lahaye, A. M. Läuchli, and A. Browaeys, Quantum simulation of 2d antiferromagnets with hundreds of rydberg atoms, *Nature* **595**, 233 (2021).
- [6] S. Ebadi, T. T. Wang, H. Levine, A. Keesling, G. Semeghini, A. Omran, D. Bluvstein, R. Samajdar, H. Pichler, W. W. Ho, S. Choi, S. Sachdev, M. Greiner, V. Vuletić, and M. D. Lukin, Quantum phases of matter on a 256-atom programmable quantum simulator, *Nature* **595**, 227 (2021).
- [7] D. Bluvstein, H. Levine, G. Semeghini, T. T. Wang, S. Ebadi, M. Kalinowski, A. Keesling, N. Maskara, H. Pichler, M. Greiner, V. Vuletić, and M. D. Lukin, A quantum processor based on coherent transport of entangled atom arrays, *Nature* **604**, 451 (2022).
- [8] H. Labuhn, D. Barredo, S. Ravets, S. de Léséleuc, T. Macrì, T. Lahaye, and A. Browaeys, Tunable two-dimensional arrays of single rydberg atoms for realizing quantum ising models, *Nature* **534**, 667 (2016).
- [9] F. M. Surace, P. P. Mazza, G. Giudici, A. Lerose, A. Gambassi, and M. Dalmonte, Lattice gauge theories and string dynamics in rydberg atom quantum simulators, *Phys. Rev. X* **10**, 021041 (2020).
- [10] S. K. Kanungo, J. D. Whalen, Y. Lu, M. Yuan, S. Dasgupta, F. B. Dunning, K. R. A. Hazzard, and T. C. Killian, Realizing topological edge states with rydberg-atom synthetic dimensions, *Nature Communications* **13**, 972 (2022).
- [11] J. C. Halimeh and P. Hauke, *Stabilizing gauge theories in quantum simulators: A brief review* (2022), [arXiv:2204.13709 \[cond-mat.quant-gas\]](https://arxiv.org/abs/2204.13709).
- [12] V. Crescimanna, J. Taylor, A. Z. Goldberg, and K. Heshami, Quantum control of rydberg atoms for mesoscopic quantum state and circuit preparation, *Phys. Rev. Appl.* **20**, 034019 (2023).
- [13] P. Scholl, A. L. Shaw, R. B.-S. Tsai, R. Finkelstein, J. Choi, and M. Endres, Erasure conversion in a high-fidelity rydberg quantum simulator, *Nature* **622**, 273 (2023).
- [14] M. Rigol, V. Dunjko, and M. Olshanii, Thermalization and its mechanism for generic isolated quantum systems, *Nature* **452**, 854 (2008).
- [15] J. M. Deutsch, Quantum statistical mechanics in a closed system, *Phys. Rev. A* **43**, 2046 (1991).
- [16] M. Srednicki, The approach to thermal equilibrium in quantized chaotic systems, *Journal of Physics A: Mathematical and General* **32**, 1163 (1999).
- [17] J. M. Deutsch, Eigenstate thermalization hypothesis, *Reports on Progress in Physics* **81**, 082001 (2018).
- [18] C. J. Turner, A. A. Michailidis, D. A. Abanin, M. Serbyn, and Z. Papić, Weak ergodicity breaking from quantum many-body scars, *Nature Physics* **14**, 745 (2018).
- [19] C. J. Turner, A. A. Michailidis, D. A. Abanin, M. Serbyn, and Z. Papić, Quantum scarred eigenstates in a rydberg atom chain: Entanglement, breakdown of thermalization, and stability to perturbations, *Phys. Rev. B* **98**, 155134 (2018).
- [20] M. D. Lukin, M. Fleischhauer, R. Cote, L. M. Duan, D. Jaksch, J. I. Cirac, and P. Zoller, Dipole blockade and quantum information processing in mesoscopic atomic ensembles, *Phys. Rev. Lett.* **87**, 037901 (2001).
- [21] N. Maskara, A. A. Michailidis, W. W. Ho, D. Bluvstein, S. Choi, M. D. Lukin, and M. Serbyn, Discrete time-crystalline order enabled by quantum many-body scars: Entanglement steering via periodic driving, *Phys. Rev. Lett.* **127**, 090602 (2021).
- [22] M. Schecter and T. Iadecola, Many-body spectral reflection symmetry and protected infinite-temperature degeneracy, *Phys. Rev. B* **98**, 035139 (2018).
- [23] D. Bluvstein, A. Omran, H. Levine, A. Keesling, G. Semeghini, S. Ebadi, T. T. Wang, A. A. Michailidis, N. Maskara, W. W. Ho, S. Choi, M. Serbyn, M. Greiner, V. Vuletić, and M. D. Lukin, Controlling quantum many-body dynamics in driven rydberg atom arrays, *Science* **371**, 1355 (2021), <https://www.science.org/doi/pdf/10.1126/science.abg2530>.
- [24] M. Pal, M. Sarkar, K. Sengupta, and A. Sen, Scar-induced imbalance in staggered rydberg ladders, *Phys. Rev. B* **111**, L161101 (2025).
- [25] S. Sachdev, K. Sengupta, and S. M. Girvin, Mott insulators in strong electric fields, *Phys. Rev. B* **66**, 075128 (2002).
- [26] K. Omiya and M. Müller, Quantum many-body scars in bipartite rydberg arrays originating from hidden projector embedding, *Phys. Rev. A* **107**, 023318 (2023).
- [27] V. Oganesyan and D. A. Huse, Localization of interacting fermions at high temperature, *Phys. Rev. B* **75**, 155111 (2007).
- [28] We have computed the fourth-order effective Hamiltonian $\hat{\mathcal{H}}_{\text{eff}}^{[4]}$ numerically by constructing the generator $i\hat{\mathcal{S}}$ in the computational basis and explicitly performing the rotation upto desired order in perturbation theory. In practice this could be continued to any order desired, however, such a numerical construction of higher-order effective Hamiltonians does not offer any insights into

the physical process the system exhibits, which closed analytical expressions can offer.

- [29] We have used a discrete time-step Runge-Kutta fourth order integrator with step size $dt = 0.005/\Omega$ for evolving the Schroedinger equation. Although this integrator does not manifestly conserve total energy or norm of the state, for all computations performed the absolute change in these quantities was less than 10^{-7} .
- [30] M. Pandey, P. W. Claeys, D. K. Campbell, A. Polkovnikov, and D. Sels, Adiabatic eigenstate deformations as a sensitive probe for quantum chaos, *Phys. Rev. X* **10**, 041017 (2020).
- [31] M. P. Zaletel, M. Lukin, C. Monroe, C. Nayak, F. Wilczek, and N. Y. Yao, Colloquium: Quantum and classical discrete time crystals, *Rev. Mod. Phys.* **95**, 031001 (2023).
- [32] V. Khemani, R. Moessner, and S. L. Sondhi, A brief history of time crystals (2019), arXiv:1910.10745 [cond-mat.str-el].
- [33] Q. Xu, J. P. Bonilla Ataides, C. A. Pattison, N. Raveendran, D. Bluvstein, J. Wurtz, B. Vasić, M. D. Lukin, L. Jiang, and H. Zhou, Constant-overhead fault-tolerant quantum computation with reconfigurable atom arrays, *Nature Physics* **20**, 1084 (2024).
- [34] A. J. Daley, Quantum trajectories and open many-body quantum systems, *Advances in Physics* **63**, 77–149 (2014).
- [35] P. Zoller, M. Marte, and D. F. Walls, Quantum jumps in atomic systems, *Phys. Rev. A* **35**, 198 (1987).
- [36] P. Zoller, Monte carlo simulation of the quantum master equation for vacuum, thermal, and squeezed reservoirs, in *Optical Society of America Annual Meeting* (Optica Publishing Group, 1992) p. MFF2.
- [37] R. Dum, P. Zoller, and H. Ritsch, Monte carlo simulation of the atomic master equation for spontaneous emission, *Phys. Rev. A* **45**, 4879 (1992).
- [38] K. Mølmer, Y. Castin, and J. Dalibard, Monte carlo wave-function method in quantum optics, *J. Opt. Soc. Am. B* **10**, 524 (1993).
- [39] A. J. Daley, J. M. Taylor, S. Diehl, M. Baranov, and P. Zoller, Atomic three-body loss as a dynamical three-body interaction, *Phys. Rev. Lett.* **102**, 040402 (2009).
- [40] T. Vovk and H. Pichler, Entanglement-optimal trajectories of many-body quantum markov processes, *Phys. Rev. Lett.* **128**, 243601 (2022).
- [41] T. Vovk and H. Pichler, Quantum trajectory entanglement in various unravelings of markovian dynamics, *Phys. Rev. A* **110**, 012207 (2024).
- [42] B. Vermersch, A. W. Glaetzle, and P. Zoller, Magic distances in the blockade mechanism of rydberg p and d states, *Phys. Rev. A* **91**, 023411 (2015).
- [43] A. Celi, B. Vermersch, O. Viyuela, H. Pichler, M. D. Lukin, and P. Zoller, Emerging two-dimensional gauge theories in rydberg configurable arrays, *Phys. Rev. X* **10**, 021057 (2020).
- [44] S. Anand, C. E. Bradley, R. White, V. Ramesh, K. Singh, and H. Bernien, A dual-species rydberg array, *Nature Physics* **20**, 1744 (2024).
- [45] J. I. Cirac, P. Maraner, and J. K. Pachos, Cold atom simulation of interacting relativistic quantum field theories, *Phys. Rev. Lett.* **105**, 190403 (2010).
- [46] A. W. Sandvik, Computational Studies of Quantum Spin Systems, *AIP Conf. Proc.* **1297**, 135 (2010), arXiv:1101.3281 [cond-mat.str-el].
- [47] L. Amico, R. Fazio, A. Osterloh, and V. Vedral, Entanglement in many-body systems, *Rev. Mod. Phys.* **80**, 517 (2008).
- [48] R. Islam, R. Ma, P. M. Preiss, M. Eric Tai, A. Lukin, M. Rispoli, and M. Greiner, Measuring entanglement entropy in a quantum many-body system, *Nature* **528**, 77 (2015).
- [49] B. Groisman, S. Popescu, and A. Winter, Quantum, classical, and total amount of correlations in a quantum state, *Phys. Rev. A* **72**, 032317 (2005).
- [50] F. Verstraete, M. Popp, and J. I. Cirac, Entanglement versus correlations in spin systems, *Phys. Rev. Lett.* **92**, 027901 (2004).
- [51] L. Zadnik and M. Fagotti, The Folded Spin-1/2 XXZ Model: I. Diagonalisation, Jamming, and Ground State Properties, *SciPost Phys. Core* **4**, 010 (2021).
- [52] I.-C. Chen and T. Iadecola, Emergent symmetries and slow quantum dynamics in a rydberg-atom chain with confinement, *Phys. Rev. B* **103**, 214304 (2021).
- [53] P. Virtanen, R. Gommers, T. E. Oliphant, M. Haberland, T. Reddy, D. Cournapeau, E. Burovski, P. Peterson, W. Weckesser, J. Bright, S. J. van der Walt, M. Brett, J. Wilson, K. J. Millman, N. Mayorov, A. R. J. Nelson, E. Jones, R. Kern, E. Larson, C. J. Carey, Í. Polat, Y. Feng, E. W. Moore, J. VanderPlas, D. Laxalde, J. Perktold, R. Cimrman, I. Henriksen, E. A. Quintero, C. R. Harris, A. M. Archibald, A. H. Ribeiro, F. Pedregosa, P. van Mulbregt, and SciPy 1.0 Contributors, SciPy 1.0: Fundamental Algorithms for Scientific Computing in Python, *Nature Methods* **17**, 261 (2020).
- [54] C.-J. Lin, V. Calvera, and T. H. Hsieh, Quantum many-body scar states in two-dimensional rydberg atom arrays, *Phys. Rev. B* **101**, 220304 (2020).
- [55] L. F. Santos and M. Rigol, Onset of quantum chaos in one-dimensional bosonic and fermionic systems and its relation to thermalization, *Phys. Rev. E* **81**, 036206 (2010).
- [56] L. D'Alessio, Y. Kafri, A. Polkovnikov, and M. R. and, From quantum chaos and eigenstate thermalization to statistical mechanics and thermodynamics, *Advances in Physics* **65**, 239 (2016), <https://doi.org/10.1080/00018732.2016.1198134>.